AGU PUBLICATIONS

JGR

Journal of Geophysical Research: Oceans

RESEARCH ARTICLE

10.1002/2016JC011653

Key Points:
- Observations of high turbulent dissipation events in the Denmark Strait Overflow plume using an AUV
- Baroclinic eddy drives entrainment by both horizontal advection and vertical mixing of warm water
- Flow-topography interaction locally induces large rates of vertical mixing

Correspondence to:
J. Schaffer,
Janin.Schaffer@awi.de

Citation:
Schaffer, J., T. Kanzow, K. Jochumsen, K. Lackschewitz, S. Tippenhauer, V. M. Zhurbas, and D. Quadfasel (2016), Enhanced turbulence driven by mesoscale motions and flow-topography interaction in the Denmark Strait Overflow plume, *J. Geophys. Res. Oceans*, *121*, 7650–7672, doi:10.1002/2016JC011653.

Received 15 JAN 2016
Accepted 16 SEP 2016
Accepted article online 21 SEP 2016
Published online 19 OCT 2016

Enhanced turbulence driven by mesoscale motions and flow-topography interaction in the Denmark Strait Overflow plume

Janin Schaffer[1], Torsten Kanzow[1,2], Kerstin Jochumsen[3], Klas Lackschewitz[4], Sandra Tippenhauer[1], Victor M. Zhurbas[5,6], and Detlef Quadfasel[3]

[1]Alfred Wegener Institute, Helmholtz Centre for Polar and Marine Research, Bremerhaven, Germany, [2]University of Bremen, Department 1 of Physics and Electrical Engineering, Bremen, Germany, [3]Institute of Oceanography, University of Hamburg, Hamburg, Germany, [4]GEOMAR, Helmholtz Centre for Ocean Research Kiel, Kiel, Germany, [5]Shirshov Institute of Oceanology, Moscow, Russia, [6]Marine Systems Institute, Tallinn University of Technology, Tallinn, Estonia

Abstract The Denmark Strait Overflow (DSO) contributes roughly half to the total volume transport of the Nordic overflows. The overflow increases its volume by entraining ambient water as it descends into the subpolar North Atlantic, feeding into the deep branch of the Atlantic Meridional Overturning Circulation. In June 2012, a multiplatform experiment was carried out in the DSO plume on the continental slope off Greenland (180 km downstream of the sill in Denmark Strait), to observe the variability associated with the entrainment of ambient waters into the DSO plume. In this study, we report on two high-dissipation events captured by an autonomous underwater vehicle (AUV) by horizontal profiling in the interfacial layer between the DSO plume and the ambient water. Strong dissipation of turbulent kinetic energy of $O(10^{-6})$ W kg^{-1} was associated with enhanced small-scale temperature variance at wavelengths between 0.05 and 500 m as deduced from a fast-response thermistor. Isotherm displacement slope spectra reveal a wave number-dependence characteristic of turbulence in the inertial-convective subrange ($k^{1/3}$) at wavelengths between 0.14 and 100 m. The first event captured by the AUV was transient, and occurred near the edge of a bottom-intensified energetic eddy. Our observations imply that both horizontal advection of warm water and vertical mixing of it into the plume are eddy-driven and go hand in hand in entraining ambient water into the DSO plume. The second event was found to be a stationary feature on the upstream side of a topographic elevation located in the plume pathway. Flow-topography interaction is suggested to drive the intense mixing at this site.

1. Introduction

The dense overflow water exiting the Nordic Seas across the sill in Denmark Strait is a major source of North Atlantic Deep Water (NADW) [*Dickson and Brown*, 1994]. The Denmark Strait Overflow (DSO) descends as a gravity plume along the Greenland continental slope and circulates cyclonically along the abyssal margins of the Irminger Basin toward the Labrador Sea [*Käse et al.*, 2003]. The intense mixing of ambient water into the DSO plume transforms the plume waters on their way downstream, which constitute the deepest layer of NADW and hence the lower limb of the Atlantic Meridional Overturning Circulation (AMOC). Variability in Denmark Strait Overflow Water (DSOW) should therefore have a direct impact on the properties and strength of the AMOC. The AMOC plays an important role in the Earth's climate system as it transports about 1.3×10^{15} W = 1.3 PW of heat northward in the subtropical North Atlantic [*Bryden and Imawaki*, 2001], which is about 25% of the total (i.e., atmospheric and oceanic) maximum heat transport. The meridional heat transport into the Nordic Seas has been estimated to be 0.3 PW [*Bacon*, 1997]. Palaeoclimate reconstructions suggest that the strength of the AMOC and the related heat transport changed dramatically throughout the Earth's history on time scales as short as a decade [*Dansgaard et al.*, 1993].

The DSOW stems from various sources in the Nordic Seas and the Arctic Ocean [*Rudels et al.*, 2002; *Våge et al.*, 2011]. Here the warm Atlantic inflow experiences strong wintertime heat loss to the atmosphere, which results in vigorous, deep-reaching convection. The cooled, convected Atlantic water mixes with fresher waters of Arctic origin to form the deep overflows [*Hansen et al.*, 2004]. On the western flank of Denmark Strait DSOW can be identified as a cold ($\Theta < 2$°C) and dense ($\sigma_\Theta > 27.8$ kg m^{-3}) bottom layer [*Dickson and Brown*, 1994]. The volume transport associated with the DSO entering the Atlantic is 3.4 ± 1.4 Sv

[*Jochumsen et al*., 2012]. On its way from the sill of Denmark Strait downstream to the southern tip of Greenland, the plume warms, freshens and increases in volume by a factor of 1.5 by the entrainment of ambient waters [*Hall et al*., 2011; *Bacon and Saunders*, 2010].

Ambient saline Atlantic Waters and fresh East Greenland Shelf Waters (EGSW) represent the main contributions to the modification and thickening of the DSO plume [*Jochumsen et al*., 2015]. In addition, some contribution might come from a less dense layer—referred to as low-salinity lid—that covers the DSO plume south of the sill of Denmark Strait [*Rudels et al*., 1999]. Hydrographic observations indicated that occasionally EGSW can be in the same density range as DSOW and sink down the continental slope [*Brearley et al*., 2012; *Falina et al*., 2012]. Numerical model simulations suggest that EGSW frequently spills over the East Greenland shelf edge, a process which is often caused by passing cyclonic ocean eddies [*Magaldi and Haine*, 2015]. In this way, EGSW may contribute to water mass modification and the downstream volume increase of the overflow.

Mesoscale eddies with time scales of 2–10 days [e.g., *Voet and Quadfasel*, 2010; *Dickson and Brown*, 1994; *Käse et al*., 2003; *von Appen et al*., 2014; *Fischer et al*., 2015; *Macrander et al*., 2007] represent the most energetic source of variability in the DSO plume transport on the continental slope off Southeast Greenland. Both the eddy-induced lateral exchange and vertical mixing driven by shear-instability at the upper interface of the plume have been shown to result in a downstream decrease in plume density and an increase in plume temperature [*Quadfasel and Käse*, 2007]. *Voet and Quadfasel* [2010] proposed that small-scale processes (e.g., internal wave breaking, Kelvin-Helmholtz instabilities) driving vertical mixing should play an important role for the warming of the DSO plume somewhere within the first 200 km downstream of Denmark Strait sill, because the observed lateral heat flux alone was too small to explain the rapid warming. The region of supposedly vigorous vertical mixing may possibly be further restricted to the interval from 100 to 200 km downstream of the sill. This reasoning is based on two observations: first, the low-salinity lid appears to be a persistent feature during the first 100 km of the descent, which should be eroded faster in the presence of strong vertical mixing. Second, based on measurements of dissipation of turbulent kinetic energy (hereafter simply referred to as dissipation) in the DSO plume at 200 km downstream of the sill, *Paka et al*. [2013] computed much smaller entrainment rates than required to explain the rapid warming of the plume observed by *Voet and Quadfasel* [2010]. *Paka et al*. [2013] therefore speculated that lateral mixing rather than vertical mixing should be the main driver of the plume modification in the first 200 km downstream of the sill. Since reliable estimates of neither vertical mixing nor lateral mixing exist in this distance interval, the question which of the two components drives the bulk of the warming in this region [see also *Jochumsen et al*., 2015] is still unresolved.

The present study is based on observations of dissipation in the interfacial layer above the DSO plume as observed by a horizontally profiling autonomous underwater vehicle (AUV) 180 km downstream of the sill in Denmark Strait. Throughout the whole study, we refer to the term interfacial layer for the thermocline separating the downstream flowing, well-mixed, cold, and dense core of the DSO plume ($\Theta < 2$°C and $\sigma_\Theta > 27.8$ kg m^{-3}) from warmer and less dense ambient water ($\Theta > 4$°C).

In this paper, we (i) present two turbulent events, (ii) discuss the associated variability in temperature, velocity, and dissipation on a range of scales from mesoscale eddies down to three-dimensional turbulence, and (iii) attempt to identify the drivers of enhanced turbulence. Although this study remains inconclusive on the dominant processes, it might represent a step forward in observing vertical mixing in the interfacial layer above the DSO plume in this area and link it exemplarily to drivers of mixing (namely, eddy-induced velocity shear and flow-topography interaction). Our observations therefore can be seen as a showcase for the conversion of energy from the plume-scale and mesoscale to three-dimensional turbulence.

2. Data and Methods

2.1. Study Area, Moored, and Lowered Measurements

The AUV missions were part of a multiplatform measurement program conducted in June 2012 aboard R/V *Maria S. Merian* (cruise MSM21/1b) between Iceland and Greenland (Figure 1) [for details see also the cruise report, *Kanzow*, 2015]. The main study area (Figures 1 and 2) was located on the continental slope off Greenland around 180 km downstream of the sill in Denmark Strait (i.e., south of Dohrn Bank and upstream of the Kangerdlugssuaq Trough).

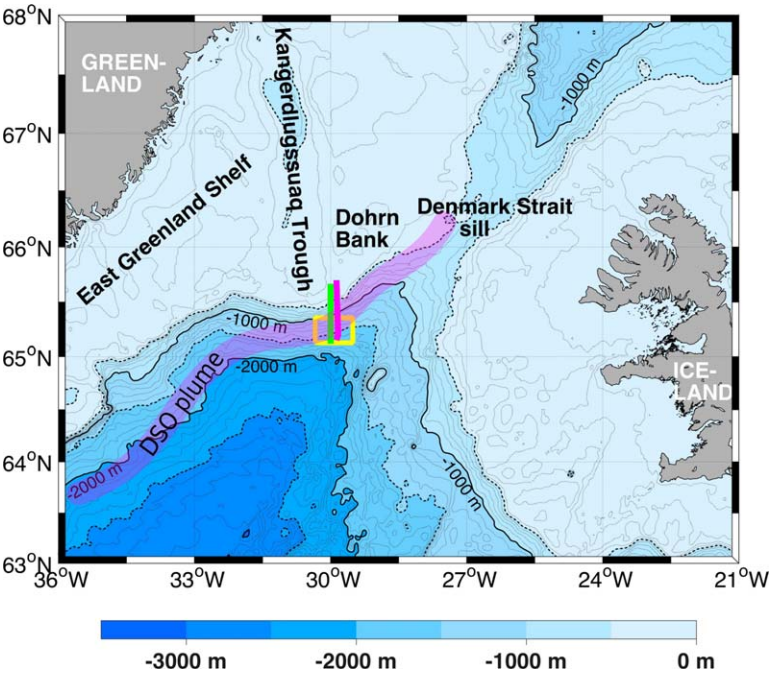

Figure 1. Map of the research area of R/V *Maria S. Merian* cruise 21/1b (MSM21/1b). Marked are the main study area expanded in Figure 2 (yellow box), and the location of CTD sections covered in June 2012 by cruise MSM21/1b (brown line) and in August 2012 by R/V *Poseidon* 437 (green line). Topographic features are labeled in black: thin dotted lines denote contours of constant depth with a spacing of 100 m, dashed lines a spacing of 500 m and thick black lines a spacing of 1000 m. The bathymetry is based on ETOPO1. The path of the DSO plume is sketched in magenta based on observations by *Girton and Sanford* [2003].

Twelve moorings equipped with a number of RDI Acoustic Doppler Current Profilers (ADCP), Aanderaa Recording Current Meters (RCM), Seabird SBE37 MicroCATs (MC; recording temperature, conductivity and pressure), and RBR temperature recorders were deployed in the main study area and carried out measurements for a period of 2 months (13 June 2012 to 6 August 2012). In this study, temperature and velocity records from the moorings M1 located in the middle of the main study area (65°14.34′N, 29°57.51′W, 1410 m) and M2 further upstream within the main study area (65°18.71′N, 29°37.20′W, 1366 m) were used to analyze the temporal variability of the overflow plume (Figure 2 and Table 1). Mooring M1 was equipped with four temperature recorders and six MC (54–194 m above the seafloor), and a 1200 kHz upward-looking

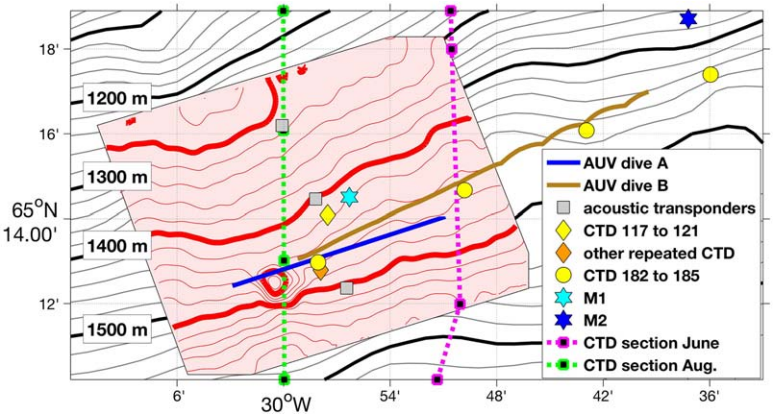

Figure 2. Map of the main study area of cruise MSM21/1b (yellow box in Figure 1). Marked are the locations of AUV missions A and B, the positions of the acoustic transponders used for the AUV navigation system, repeated CTD stations close to the AUV tracks and other CTD stations used in this work, mooring sites M1 and M2 as well as CTD sections across the plume obtained during June 2012 and August 2012. The depth contours shown by thick and thin black lines have a spacing of 100 m and 20 m, respectively, and are based on ETOPO1. The area shaded in light red shows a map based on a multibeam echo sounder survey carried out during cruise MSM21/1b (using red depth contours, respectively).

Table 1. Technical Details of the Instruments Used in the Moorings M1 and M2

Mooring	Instrument and Company	Sampling Interval (s)	Parameters	Height Above Ground (m)	Depth (m)
M1	ADCP 1200 kHz Teledyne RDI	5	*u*, *v*	123	1297
				155	1265
				124	1296
M1	SBE37 MicroCAT Seabird	20	*T*, *S*, *P*	105	1304
				109	1311
				102	1318
				65	1355
				205	1215
M1	Temperature recorder RBR	600	*T*	145	1275
				135	1285
				97	1323
M2	RCM 11 Aanderaa	600	*u*, *v*	24	1339

ADCP (123 m above the seafloor, using 32 bins and a bin size of 0.5 m). The depth of all moored sensors is variable due to knock-downs of the mooring during strong current speeds. During these times pitch and roll reading of the moored ADCP stalled at high values (roll $\leq -26.8°$ or roll $\geq 28.8°$ or pitch $\leq -28.9°$ or pitch $\geq 26.5°$) and we expect the ADCP-inferred velocities to be not reliable. At the mooring site M2 velocity records were obtained by a RCM at 24 m above the seafloor (details in Table 1). Throughout the study ADCP-inferred current speeds refer to absolute velocities calculated based on horizontal (v_x, v_y) and vertical (v_z) velocity components $\left(|\vec{v}|=\sqrt{v_x^2+v_y^2+v_z^2}\right)$, while for all other devices horizontal velocity components were considered only.

In total, 38 regular conductivity-temperature-depth/lowered ADCP casts (CTD/LADCP) and three yo-yo CTD/LADCP casts were carried out in the main study area. The positions of the CTD/LADCP stations used in this work are shown in Figure 2. A standard CTD SBE 911+ system equipped with a pressure sensor and two sets of temperature, conductivity, and oxygen sensors was used, sampling at 24 Hz. The conductivity and oxygen sensors were calibrated using water samples taken from Niskin bottles, resulting in very high accuracy data (salinity bottle—sensor deviation of 0.0014 rms). All salinities given in this work are reported on the practical salinity scale (PSS-78). The processed CTD profiles yield a vertical resolution of 1 dbar extending from the surface to approximately 10 m above the seafloor.

During all casts a LADCP system comprising two 300 kHz ADCPs was mounted on the CTD rosette system, with one device oriented upward and the other one downward, for measurements of vertical profiles of velocities. The data was processed following *Visbeck* [2002] with a vertical resolution of 10 m and an accuracy of 4 cm s^{-1}, and is constrained by the ship-ADCP.

2.2. AUV-Based Measurements

To a large extent, this study is based on observations of turbulence carried out aboard a horizontally moving AUV. The AUV *Abyss*—a REMUS 6000—was operated using the same setup as described by *Tippenhauer et al*. [2015]. A pumped Seabird 49 FastCAT CTD system measured hydrographic data at a frequency of 4 Hz, while the Paroscientific pressure sensor was operated at 1 Hz. In addition to the standard sensors, a MicroRider 6000 horizontal microstructure profiler (MSP) from Rockland Scientific Inc. was attached near the bow of the AUV (Figure 2 in *Tippenhauer et al*. [2015]). In this setup, the MSP was equipped with two airfoil microstructure velocity shear probes and two fast-responding microstructure thermistors (FP07), both operating at 512 Hz [for more details see *Tippenhauer et al*., 2015].

The AUV used a combination of three different navigation systems. The initial position of the vehicle prior to each dive is obtained by GPS and is used to align the Kearfott T-24 Inertial Navigation System (INS) at the sea surface. Once diving, the vehicle initially relied on the INS for navigation purposes. Within a distance of 200 m from the seafloor—which is where the AUV mainly operated—position information was obtained from the Doppler Velocity Log (DVL), a downward-looking ADCP operated in bottom track mode. In addition, the long baseline acoustic navigation (LBL) was used to further improve positioning. LBL relied on acoustic triangulation using three moored transponders positioned along a cross-slope section with a spacing of 4 km (Figure 2) in order to ensure that the AUV would be able to follow isobaths inside the LBL range with high accuracy.

Corrections of the position data needed to be performed when the navigation system switched between the INS, DVL and the more accurate LBL systems. During the AUV missions position offsets between these systems ranged from few tens of meters to 440 m. All position data, which showed differences larger than 15 m between two consecutive points, were adjusted using an interpolation technique described by *Schaffer* [2013].

The speed of the AUV *over the ground* can be calculated from the (corrected) positions of the AUV provided by the onboard navigation system. The speed of the AUV *through the water* can be calculated from the AUV propeller rotation rate. The propeller rotation rate has been kept constant throughout the dives and translates to a constant speed of the AUV of 1.6 m s^{-1} *through the water*—no matter whether the AUV went against the flow or in the direction of the flow. Thus any propeller-generated turbulence should not have a larger impact on our measurements, even when the AUV heads against the flow. The speed of the AUV *through the water* is equivalent to the flow past sensor. The absolute current velocity can be obtained from the difference of the AUV speed *over the ground* and the AUV speed *through the water*.

2.2.1. Data Processing and Calibration of AUV-CTD Sensor Data

The thermistor of the SBE 49 CTD (AUV-CTD) was used as a recursive conductivity filter to remove the differences in response times between the thermistor (response time less than 1 s) and the conductivity cell thermal mass error (roughly 19 s) [*Johnson et al*., 2007]. For the corrections, we relied on the equations and calibration constants as provided by the Seabird Software (*Sea-Bird Electronics*, 2012) for the SBE 49 CTD based on the experiments of *Lueck* [1990].

The temperature and conductivity data measured by the AUV-CTD were subsequently smoothed using a butterworth low-pass filter with a cutoff frequency of 0.125 Hz. For a typical speed of the AUV through the water of 1.6 m s^{-1}, this translates into a spatial low pass filter with a cutoff wavelength of 12.8 m. With observations of small-scale variability being a core interest of this study, this cutoff represented a reasonable compromise between the need to remove high-frequency noise (particularly in salinity) and the need to retain sufficient energy in the turbulent regime as will be shown later.

The salinity measurements of the AUV-CTD system were corrected for an offset obtained by a comparison with the calibrated lowered CTD measurements. We assumed that temperature and pressure measurements of the AUV-CTD were accurate, so that deviations in Θ-S space between both systems can be used to correct salinity (conductivity) of the AUV system. Relying on 34 lowered CTD profiles, close to the AUV tracks, a time-independent and depth-independent offset of $\Delta S = 0.005$ was added to all AUV-based salinities used in this study.

All AUV-CTD data were interpolated onto a time grid with a time step of 4 s, resulting in a spatial grid size of about 6.4 m.

2.2.2. Microstructure Data

The dissipation of turbulent kinetic energy (ε) was computed from velocity shear data. Spectra of the velocity shear data (Φ) were integrated by assuming isotropic turbulence [*Taylor*, 1935; *Oakey*, 1982]. Isotropy may be assumed if $\varepsilon > 200 \cdot \nu N^2$, with N being the buoyancy frequency and ν the kinematic viscosity [*Gargett et al*., 1984; *Yamazaki and Osborn*, 1990]. The buoyancy frequency ($N^2 = 4\times10^{-5}$ s^{-2}, in the interfacial layer) and kinematic viscosity ($\nu < 1.82\times10^{-6}$ m^2 s^{-1}) were determined from CTD profiles. Hence, isotropy may be assumed for dissipation rates exceeding 10^{-8} W kg^{-1}.

The dissipation rate of turbulent kinetic energy (TKE) is commonly computed invoking the assumption that Φ has the shape of the universal Nasmyth spectrum, which was determined by *Nasmyth* [1970] and reported by *Oakey* [1982]. The dissipation rate is estimated by integrating these spectra. The methods of computing horizontal wave number shear spectra, reducing the noise induced by vibrations from the propeller and rudder systems of the AUV, as well as finding appropriate limits for the integration of shear spectra are described by *Tippenhauer et al*. [2015]. The contamination from the propeller induced TKE on our dissipation rates is small because the microstructure profiler is placed at the AUV's nose while the propeller induces turbulence at the stern of the AUV. As described in more detail in *Tippenhauer et al*. [2015], the influence of the vibrations can be reduced by using a filter developed by *Goodman et al*. [2006]. Using this filter, the spectra can be sufficiently "cleaned" from contaminations such that the dissipation rate can be computed by integrating the spectra [*Tippenhauer et al*., 2015].

The noise level for our data set was estimated to be about $\varepsilon_n = 2\times10^{-9}$ W kg^{-1} compared to $\varepsilon_n = 2.5\times10^{-9}$ W kg^{-1} and $\varepsilon_n = 7\times10^{-10}$ W kg^{-1} for the data sets of *Tippenhauer et al*. [2015]. The

Table 2. Details of the AUV Missions A and B Carried Out in the Main Study Areaa

Dive ID	Launch Date	Launch (UTC)	Recovery (UTC)	Leg	Mean Depth/Height Above Flat Average Seafloor (m)	Start Time (UTC)	End Time (UTC)
A	12–13 June 2012	22:01	11:14	1	1340/125	23:11	23:44
				2	1415/50	23:50	1:10
				3	1365/100	1:13	2:18
				4	1340/125	2:21	2:57
				5	1315/150	2:58	4:46
				6	1265/200	4:49	6:36
				7	1215/250	6:39	8:24
				8	1165/300	8:26	9:52
B	20 June 2012	09:18	16:08	1	1350/91	10:07	15:05

dissipation rates computed from the individual shear probes were in good agreement, therefore we use dissipation rates from only one of the shear probes for our analysis.

The two fast-response thermistors were used to analyse the temperature fine structure related to turbulence. The temperatures of the two fast-response thermistors showed a correlation of $r \geq 0.9993$. In comparison with temperature measurements from the calibrated regular AUV-CTD (i.e., SBE49), offsets of 4.3 and 3.9°C were observed. The time series of the fast-response thermistors were corrected for the offsets applying linear regressions of the two signals to the signal of the AUV-CTD.

2.2.3. AUV Missions

In total, eight AUV dives were completed inside the main study area in June 2012. During all missions the AUV was programmed to dive at constant depth levels along straight legs approximately parallel to chosen isobaths with a constant speed of 1.6 m s^{-1} *through the water* to capture horizontal property changes on scales down to a few meters. Structures larger than 12 m are resolved by the low-passed "slow" SBE49 CTD, whereas structures smaller than 12 m should be resolved by the fast thermistors, i.e., fine-scale changes in salinity are not detected. Five of eight dives were carried out successfully. Aborts on three dives were caused by strong counter currents the AUV experienced in the DSO plume, which made the AUV fail to reach its waypoints on schedule.

In this study, we present measurements collected during AUV dives A and B only (Figure 2 and Table 2), where both the hydrographic variability and the dissipation rates were observed to be enhanced. Periods when the AUV changed its heading direction (in order to turn around) or accelerated to move from one depth level to the next upward, have been discarded in this study. Thus, only data from the straight legs at constant depth are considered.

During dive A the AUV carried out measurements approximately along the 1480 m isobath at the Greenland continental slope (Figure 2) resolving the plume on seven depth levels between 50 and 300 m above the flat ground (Table 2). Dive B was carried out for the duration of 5 h at a constant depth level of 91 $\pm$ 1 m above the seafloor in the interfacial layer between the plume and ambient water, i.e., on the upper boundary of the plume, as will be shown later (Figure 4). Heading toward northeast (i.e., against the DSO plume), the AUV was approximately following the 1460 m contour line of the Greenland continental slope and covered a 17 km long horizontal profile above the seafloor corresponding to a distance of 28.8 km *through the water* (Figure 2).

2.3. Methods: Isotherm Slope Spectra

The aim of our study is to link mesoscale and submesoscale variability in the DSO plume to amplitudes of variability on spatial scales much smaller than those, i.e., to three-dimensional isotropic turbulence. Ultimately, this might represent a way forward in understanding the processes underlying the conversion of energy from larger scales to those on which kinetic energy is finally dissipated. Based on the fact that turbulent motion generates small-scale fluctuations in scalar properties, spectra of scalar properties in the ocean such as temperature may be used in order to distinguish between different regimes and amplitudes of turbulence [*Klymak and Moum*, 2007a]. In this context, an advantage of horizontal profiling of temperature—as performed by the AUV—over vertical profiling is, that the signature of turbulence extends to larger scales in the horizontal domain than in the vertical one [*Klymak and Moum*, 2007b].

In order to resolve small-scale temperature fluctuations, we will analyze both, data from the standard AUV-CTD system and from the more sensitive fast-response thermistor (FP07) operated in the MSP aboard the AUV. We followed the procedure described by *Klymak and Moum* [2007a] to compute isotherm slope spectra ($\Phi_{d\zeta/dx}$) from the horizontal measurements of temperature, with ζ representing the vertical isotherm displacement and $d\zeta/dx$ the horizontal slope thereof. The computation of displacement spectra yield the advantage, that the measurements obtained in different background stratifications become more comparable than when using temperature spectra. This procedure is also preferable for the computation of dissipation rates of turbulent kinetic energy from temperature data [*Klymak and Moum*, 2007a]. In addition, $\Phi_{d\zeta/dx}$ allow for a much better (visual) discrimination between both the different subranges of turbulence and the internal wave range than the more common horizontal temperature spectra. From theory we expect to find the slopes of the isothermal displacement slope spectra of the internal wave range, and the turbulent inertial-convective and inertial-diffusive subranges to exhibit wave number ($k-$) dependencies of k^{-1} to k^0, $k^{1/3}$, and k^1, respectively [*Klymak and Moum*, 2007a].

To compute $\Phi_{d\zeta/dx}$, the horizontal temperature records were transferred from the time domain to distance (*through the water*) using the constant velocity of the AUV *through the water* (i.e., 1.6 m s^{-1}). Based on these, temperature wave number spectra were computed using 2850 m and 180 m long segments for the AUV-CTD and the MSP fast-response thermistor data respectively, with an overlap of 50%.

Subsequently, the temperature spectra were transformed to isotherm slope spectra by

$$\Phi_{d\zeta/dx}(k_x) = (2\pi k_x)^2 \left\langle \frac{dT}{dz} \right\rangle^{-2} \Phi_T \quad [\mathrm{cpm}^{-1}] \tag{1}$$

following *Klymak and Moum* [2007b]. The background temperature gradient $(dT/dz)^2$ was computed over a vertical scale of 50 m individually for each segment based on lowered CTD profiles carried out close to and during each of the AUV legs.

Although the AUV had been programmed to dive at constant depth levels, small variations in the depth values (e.g., standard deviation of 0.2 m and maximum amplitudes of 1.4 m along dive B) were observed. This it two to three orders of magnitudes smaller compared to typical isotherm displacements on top of the DSO plume, as will be shown later (Figures 5b and 8). Nonetheless, the upward and downward motion of the vehicle may cause artificial temperature fluctuations not related to isotherm displacements. In order to test the degree of contamination of $\Phi_{d\zeta/dx}$ by vertical displacements of the AUV, the AUV-based depth (pressure) data are used. The depth spectrum (which describes the variance distribution of vertical AUV displacements) was multiplied by $(2\pi k)^2$ to obtain the displacement slope spectrum ($\Phi_{dz/dx}$) of the AUV, which can be directly compared to $\Phi_{d\zeta/dx}$. It turned out that $\Phi_{d\zeta/dx}$ is at least one order of magnitude larger than

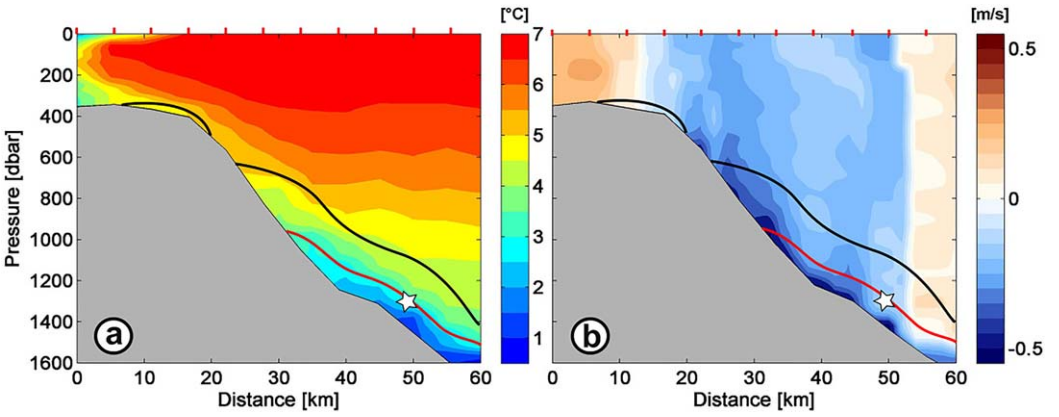

Figure 3. (a) Smoothed temperature and (b) downstream velocity sections computed from CTD and LADCP profiles conducted in June 2012 in the research area during cruise MSM21/1b. The red line represents the upper boundary of the DSO plume (determined by the 27.8 kg m^{-3} isopycnal) for this cruise and the black line illustrates the same isopycnal at this section for the R/V *Poseidon* cruise in August 2012. The positions of the stations are indicated as red marks at the top of the plots. Negative velocities represent flow to the southwest. The white star marks the approximate position of the ADCP at mooring site M1.

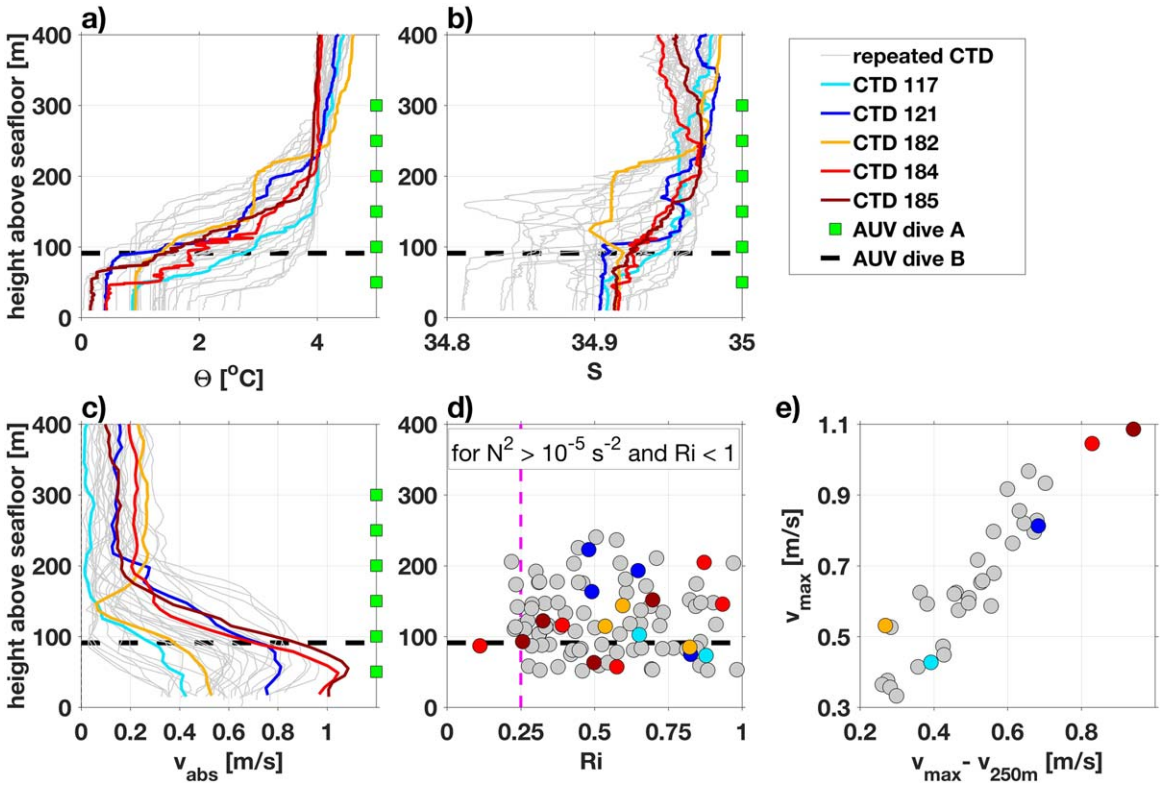

Figure 4. (a) Vertical profiles of potential temperature, (b) salinity, (c) absolute velocity, and (d) Richardson numbers as a function of height above the seafloor, and a plot of the DSO plume speed (maximum absolute velocity, v_{max}) versus the velocity shear ($v_{max} - v_{250m}$, where v_{250m} is the mean absolute velocity between 240 and 260 m above the seafloor) (e). Highlighted in colors are CTD profiles taken during AUV dive A (light/dark blue) and dive B (yellow/red/dark red). The black dashed line indicates the depth at which AUV dive B was carried out. The green squares mark the leg depths covered during AUV dive A.

$\Phi_{dz/dx}$ for the entire wave number range of the spectra (not shown). Therefore, the contamination of $\Phi_{d\zeta/dx}$ by vertical movements of the AUV can be considered to be negligible in this study.

3. Results

3.1. AUV Measurements in the Interfacial Layer Above the DSO Plume

The dense DSO plume can be seen in Figure 3, representing cross-slope hydrographic and current sections acquired in June 2012 aboard R/V *Maria S. Merian*; additionally included is the overflow plume location for a subsequent cruise in August 2012 with R/V *Poseidon* (see maps in Figures 1 and 2). In August 2012 the plume covered a broad bottom layer and dense water was also present on the continental shelf which was not the case in June 2012. This exemplifies that the horizontal and vertical extent of the plume is highly variable.

In agreement, repeated CTD/LADCP profiles taken in the main study area (Figure 2) within nine days show the cold, well-mixed core of the DSO plume with a thickness ranging between 30 and 130 m (Figures 4a and 4b). Within the bottom mixed layer the potential temperature varied by more than 2°C and the salinity by about 0.1 between the different profiles. Maximum current speeds cover the range from 0.4 up to 1.1 m s^{-1} (Figure 4c). Above the mixed layer, strong vertical temperature and velocity gradients indicate the interface between the DSO plume and the ambient water.

A striking feature of the velocities in the study area is that they exhibit not only a *time mean* bottom-intensified flow, but the *time variable* motions are also bottom-intensified. This can be seen by a positive correlation between the velocity within the core and the vertical gradient of horizontal velocity above it (Figure 4e). On time scales shorter than 9 days the core velocities may therefore be largely modulated by baroclinic, bottom-intensified motions. This observation may have important implications for the impact of mesoscale variability on the entrainment of ambient water into the plume, as discussed later.

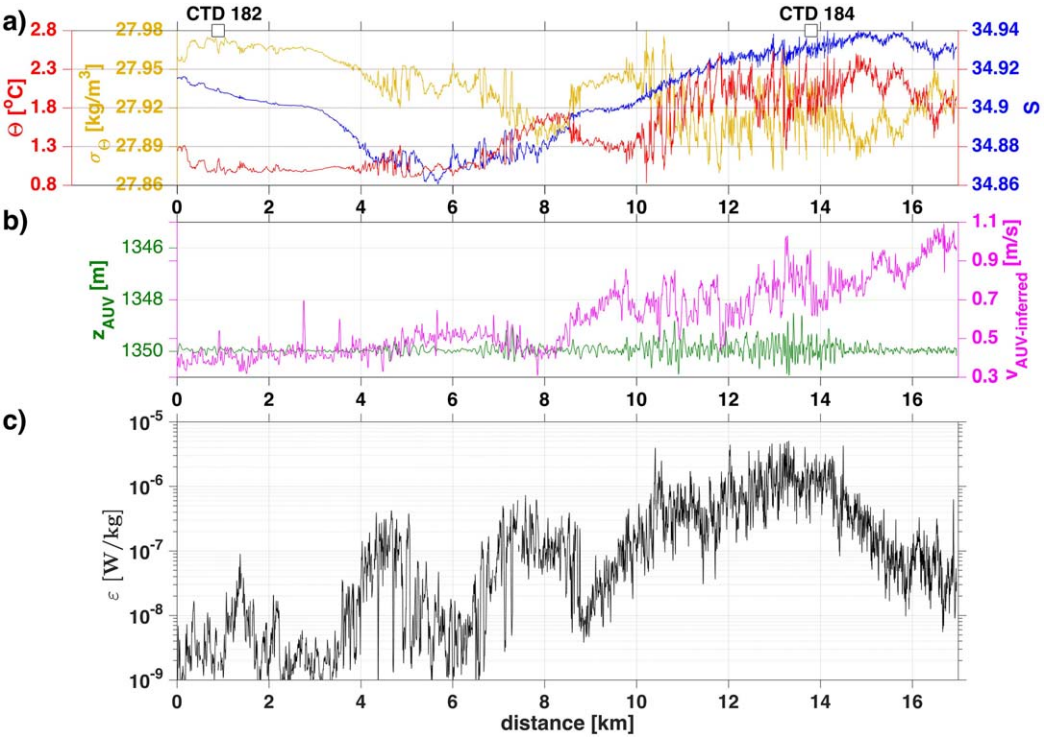

Figure 5. Hydrographic and dissipation data during the horizontal profile of AUV dive B. (a) Potential temperature (red), salinity (dark blue), and potential density (yellow); (b) the AUV depth (green) and AUV-inferred current velocity (magenta), i.e., the difference between the AUV speed *over the ground* and the AUV speed *through the water*. (c) The dissipation rates from the microstructure measurements. In all plots, the horizontal axes gives the distance of the AUV to the southwestern-most point of the deep leg (see Figure 2). The corresponding locations of CTD profiles 182 and 184 taken at the same time (and shown in Figure 4) are marked on the top of Figure 5a by white squares.

From the CTD/LADCP profiles taken during the AUV missions A (CTD profiles 117, 121) and B (CTD profiles 182, 184, 185), it can be seen that both the leg of dive B and some legs of dive A taken near 100 m above the seafloor were (intentionally) located inside of the interfacial layer above the well-mixed DSO plume (Figures 4a–4c). In the following we study the AUV-measurements in the interfacial layer in more detail.

3.2. Measurements Near the Edge of an Energetic Eddy

3.2.1. Hydrographic Variability, Dissipation Rates, and Current Speeds

Pronounced hydrographic variability is observed along the horizontal profile of AUV dive B (Figure 5a) carried out at a depth of 1349 m, i.e., 91 m above the seafloor. While during the first half of the leg (in the interval between 0 and 10 km) rather calm conditions are observed, strong high-frequency fluctuations in both temperature and salinity are found in the second half of the dive (Figure 5). High-pass filtered temperature time series (1 min cutoff period, Θ_{filt}) yield a standard deviation of $\pm$0.2°C in the interval between 10 and 14.5 km, i.e., 4 times larger compared to the first half of the leg. This change goes along with an overall warming of about 1°C and a doubling of the plume velocity to 1.0 m s^{-1} (Figures 5a and 5b). Salinity instead first decreases up to a distance of 6 km by 0.06 and subsequently gradually increases by 0.08 until the end of the leg. The enhanced high-frequency temperature fluctuations coincide with enhanced dissipation rates of O(10^{-6}) W kg^{-1} in the segment between 10 and 14.5 km compared to O(10^{-8}) W kg^{-1} between 0 and 4 km (Figure 5c). At the same time the AUV depth fluctuates with an amplitude 10 times larger than that present during the first half of the dive (Figure 5b).

In general, all hydrographic data obtained along the track are contained in the typical range of DSOW with potential densities ranging between 27.87 and 27.97 kg m^{-3} (Figures 5a and 6). However, strong deviations from a straight line in Θ-S space are observed, which indicate that at least three different source water masses are required to explain the observations. The evolution of the water mass properties indicates a gradually increasing contribution of low-salinity East Greenland Current waters within the DSO plume

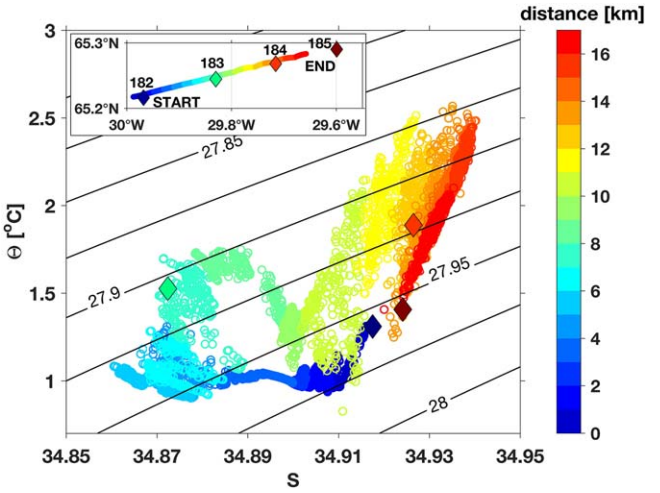

Figure 6. Θ-*S*-diagram collected during AUV dive B. The small inset illustrates the track of the AUV and the locations of the CTD stations (diamonds, casts 182–185). Colors indicate the distance of the AUV and CTD stations from the starting point of the AUV track in the southwest. The AUV dives along the slope heading northeast against the mean flow direction. The same color range as for the inset is used in the Θ-*S*-diagram in order to illustrate from which location the data originates. Circles indicate data of the AUV-CTD. Diamonds mark Θ-*S*-data averaged over a depth range between 80 and 100 m above the seafloor from four lowered CTD profiles (i.e., in the depth range of the AUV). The CTD profiles (casts 182, 184, 185) are shown in Figure 4, respectively.

during the first half of the dive (Figure 6, from blue to green colors), while during the second half of the dive a shift to more warm and saline Atlantic water can be seen [cf. *Jochumsen et al.*, 2015]. The temperature and salinity changes do not compensate each other entirely in terms of density (Figure 6). The observed temperature fluctuations dominate density variations at distances from 6 km onward. This is true both for the high-frequency variations and the more gradual changes. Salinity variations instead appear to dominate density variations between 0 and 6 km. Θ-*S* properties from lowered CTD casts carried out during the dive (Figure 6, diamonds) are in agreement with those obtained by the AUV-CTD.

Lowered CTD/LADCP profiles (Figure 4) carried out during AUV dive B show strong changes in the hydrographic properties and plume velocities supporting the AUV-based observations. As will be discussed later, these changes are thought to correspond to the passage of a mesoscale eddy. The temperatures in the bottom mixed layer of the plume rise along the upstream path taken by the AUV from 0.1 to 1°C, while the salinity remains roughly constant at $S = 34.92$ (Figures 4a and 4b). The plume velocities differ greatly: at the downstream profile 182 the core velocity is 0.5 m s^{-1} compared to 1.1 m s^{-1} at the upstream profiles 185 (Figure 4c). The profiles clearly show the strong decline of the velocity outside of the bottom plume and no indication for a surface signature corresponding to an increase in plume speed (Figure 4e).

3.2.2. *Ri* Numbers

At profile 184, we observe strong temperature fluctuations (Figure 4a) and a strong vertical shear in horizontal velocities in the interfacial layer (Figures 4c and 4e). Aiming at studying on the likelihood of Kelvin-Helmholtz instabilities to initialize turbulence, we calculated Richardson numbers defined by $Ri = \frac{N^2}{S_v^2}$, where $N^2 = -\frac{g}{\rho}\frac{\partial \bar{\rho}}{\partial z}$ is the buoyancy frequency and $S_v^2 = \left(\frac{\partial v_x}{\partial z}\right)^2 + \left(\frac{\partial v_y}{\partial z}\right)^2$ the velocity shear. It is desirable to evaluate *Ri* numbers at spatial scales larger than typical Ozmidov length scales defined by $L_O = \left(\frac{\varepsilon}{N^3}\right)^{\frac{1}{2}}$ in order to exclude turbulent motion. Based on the stratification and dissipation rates measured in the DSO plume from lowered CTD profiles and AUV-based microstructure measurements respectively, we calculated typical Ozmidov scales (ranging between 6 and 32 m). By this a 30 m running mean was applied to N^2 and S_v^2 to subsequently compute *Ri* numbers based on lowered CTD/LADCP measurements. Within the interfacial layer we observe critical *Ri* numbers less than 0.2 about 90 m above the ground at profile 184 (Figure 4d). The value of *Ri* being smaller than 0.25 indicates that the velocity shear (obtained on a 30m scale) is strong enough to generate turbulent mixing across the density gradient. This indicates that exactly here, entrainment of ambient water is going on. This CTD/LADCP cast was taken at the same time and in the vicinity of the AUV-based measurements of enhanced dissipation rates (Figure 5c) and during the passage of an eddy (as will be shown below).

3.2.3. Small-Scale Temperature Variability

The simultaneous occurrence of high-frequency temperature fluctuations (0.2°C rms) and enhanced dissipation rates of $O(10^{-6})$ W kg^{-1} observed during the second half of dive B (Figures 5a and 5c) can be expected to induce pronounced heat fluxes across the interfacial layer into the core of the DSO plume. In the following, we analyze the temperature variances and scales of variability in more detail. By using the fast-response thermistor from the MSP rather than the AUV-CTD record we can extend shortest resolved time scales to 0.02 s corresponding to spatial scales of 3.2 cm. Although our measurements are not capable to

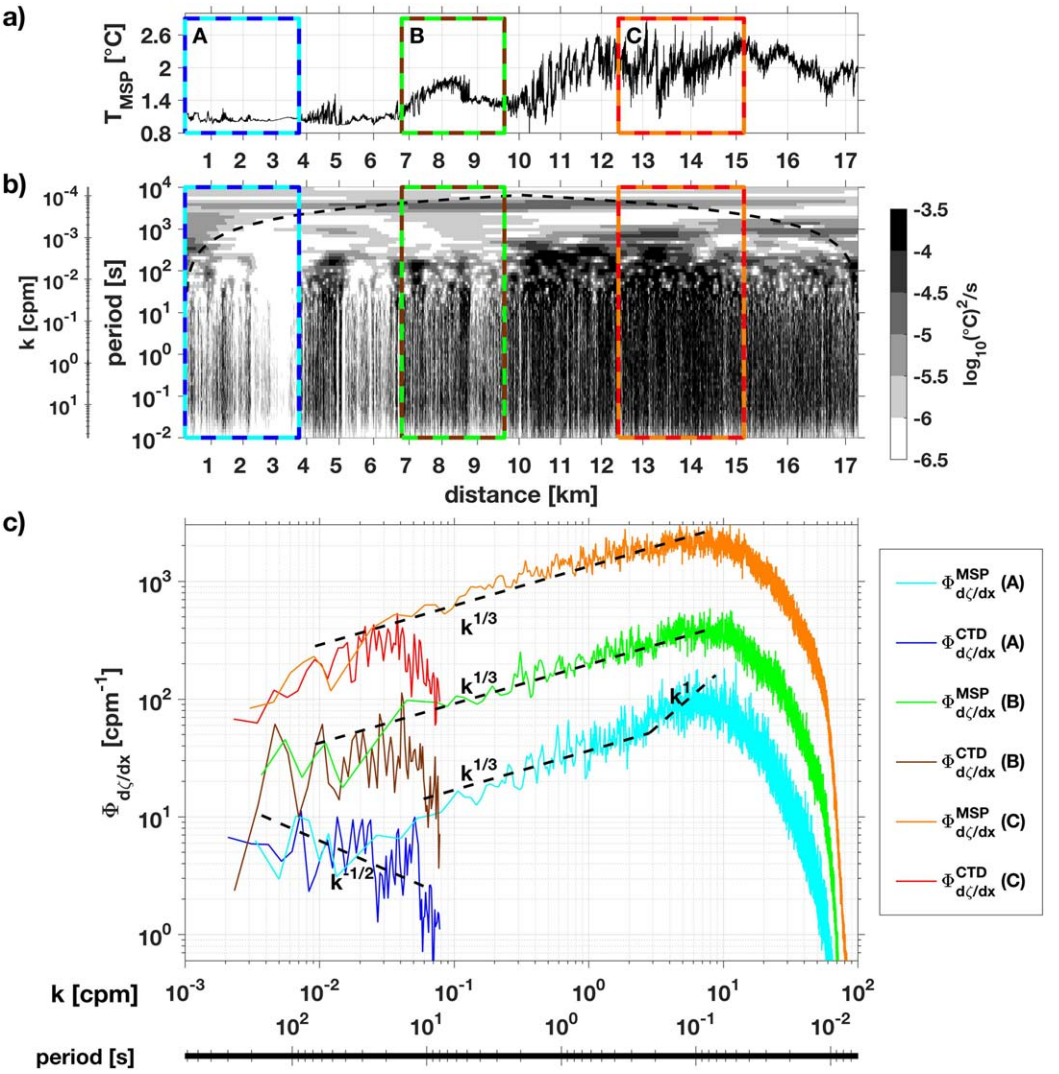

Figure 7. (a) Temperature time series from the fast-response thermistor of the MSP, (b) wavelet power spectral density computed from the fast-response thermistor temperature time series, and (c) isotherm slope spectra during AUV dive B. (b) We used a downsampled fast-response thermistor temperature time series with 170 Hz resolution. For purposes of visualization the colorbar of wavelet power spectral density is restricted on the lower end (minima extend to $O(-14)^\circ\ C^2\ s^{-1}$). On the left, the additional axes give the corresponding wave numbers in cpm. The black dashed line indicates the cone-of-influence [*Torrence and Compo*, 1998]. (c) The isotherm slope spectrum ($\Phi_{d\zeta/dx}$) of each segment is calculated from the fast-response thermistor (light blue, green, and orange lines) and the AUV-CTD (dark blue, brown, and red). The black dashed lines show the expected slopes of the equilibrium spectra in the internal wave range ($k^{-1/2}$), the inertial-convective subrange ($k^{1/3}$), and the inertial-diffusive subrange (k^1) of turbulence, respectively. The wave numbers correspond to *distance through the water* (as opposed to *distance above the ground*).

resolve scales where kinetic heat is turned into heat, they can resolve the energy transition between internal waves and turbulence.

Wavelet analysis of the fast-response thermistor temperature time series obtained during AUV dive B reveals the largest temperature variance density of $O(10^{-2}\ (^\circ C)^2\ s^{-1})$, between 10 and 14.5 km (Figure 7b). Here the amplitude of temperature variance is three orders of magnitude higher than that of the background signal (present between 0 and 4 km of the AUV dive). The variance is dominated by fluctuations found on wave numbers between 0.002 and 20 cpm (corresponding to wavelength between 0.05 and 500 m, and time scales of 0.03 s to 5 min) while it is two to three orders of magnitude smaller during the first part of the AUV dive, i.e., before 10 km.

In order to analyse spatial scales that correspond to the turbulent subranges, which has not been done for the DSO plume before, we calculated isotherm slope spectra (Figure 7c). We use the spectra not only to

describe temperature variance wave number characteristics but also to find indications for the presence of internal waves, and to figure out whether a transition between internal waves and turbulence is observed. We compared three different segments of AUV dive B. The segments A, B, and C were chosen to capture temperature fluctuations associated with weak, moderate, and strong turbulent dissipation (Figures 7a and 7b), respectively. $\Phi_{d\zeta/dx}$ computed using the fast-response thermistor data of the MSP looks almost identical to that obtained by the AUV-CTD temperature time series for $k < 0.04$ cpm (Figure 7c). The dropoff in the spectra based on CTD-temperatures is in part artificially caused by the low-pass filter we applied at $k > 0.08$ cpm. The spectra derived from the fast-response thermistor extend to much higher wave numbers and are therefore more suitable to distinguish the turbulence subranges.

Isotherm slope spectra derived from the fast-response thermistor data display the largest variance levels in segment C and the lowest ones in segment A. This agrees with the amplitudes of dissipation rates in the segments, respectively (Figure 5c). The shapes of the spectra from the segments B and C are very similar to one another. In contrast, the shape of the least energetic segment A shows a different shape toward the shortest and longest extend of the wave number range. In the range from 0.01 cpm $\leq k \leq 7$ cpm (corresponding to wavelengths of 100 to 0.14 m) the slopes are largely consistent with those of the inertial-convective subrange of turbulence (parallel to $k^{1/3}$) [*Klymak and Moum*, 2007a] for the energetic segments B and C (Figure 7c). The inertial-convective subrange of turbulence for the least energetic segment A extends from 0.04 to 3 cpm. For $k > 10$ cpm, the energy drops off in all spectra. Based on theory [*Klymak and Moum*, 2007a], we expect the spectra to show a transition to the inertial-diffusive subrange (parallel to k^1) at higher k. No indication for the presence of the k^1 dependence at $k > 3$ cpm is found for segments B and C. For the least energetic segment A, a weak indication of the presence of the inertial-diffusive subrange of turbulence between 3 and 8 cpm is found, in the sense that the slope first increases before the dropoff. In the low wave number limit we expect the spectra to make a transition to the internal wave subrange (proportional to $k^{-1/2}$). We find indication of the $k^{-1/2}$ dependence at $k < 0.04$ cpm in segment A and possibly even in segment B, however not in the most energetic segment C. We will return to these aspects in the discussion (section 4.1).

3.2.4. (Sub)Mesoscale Variability

The role that eddies play in laterally entraining warm ambient water into the DSO plume has been highlighted by *Voet and Quadfasel* [2010]. It is thus worthwhile to look in more detail at the interplay between mesoscale eddies, plume-ambient water exchange and diapycnal mixing based on the turbulent event encountered during dive B. We start by describing the DSO plume conditions in the work area based on moored measurements.

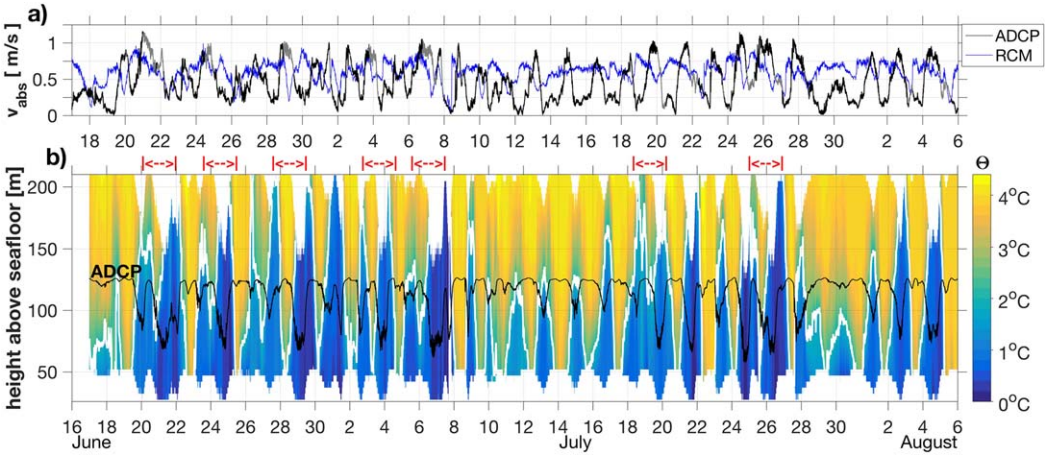

Figure 8. Moored time series of (a) absolute current velocity (v_{abs}) from the ADCP at mooring site M1 and RCM at mooring site M2, and (b) potential temperatures (Θ) at mooring site M1. The depth of all moored sensors are variable due to knock-downs of the mooring during strong current speeds and we expect the ADCP-inferred velocities to be not reliable (gray lines in the velocity record, plot a). In Figure 8b, the time evolution of potential temperatures is obtained by vertical interpolation between 10 temperature sensors of the M1 mooring (see Table 1 for instrument details). Here we marked the ADCP depth (black line), the 2° isotherm (white line) and the periods of strong eddy events (red bars).

The ADCP-based velocity time series at the central mooring M1 (see map in Figure 2 for the position of the mooring) frequently shows values between 0.8 and 1.1 m s^{-1} (Figure 8a). Apart from a weak peak caused by the semidiurnal tide, spectral analysis revealed a much more pronounced peak at a period of 1.6 days (not shown). This peak is associated with the passage of mesoscale eddies [e.g., *Voet and Quadfasel*, 2010]. The moored time series recorded by the RCM further upstream and upslope at M2 (Figure 2) shows less pronounced peaks in velocity, but the mean absolute velocity is larger, i.e., 0.60 $\pm$ 0.14 m s^{-1} in comparison to 0.46 $\pm$ 0.26 m s^{-1} at M1. The observations of mean current velocities suggest, that our mooring site M1 is located on the downslope side of the DSO plume, which is also expected by its position at the 1420 m isobath (Figures 1 and 3). The larger standard deviations found at M1 cannot be explained by meandering motions of the plume but rather indicate the regular passage of eddies on the downslope side of the DSO plume.

We like to point out, that the observed differences in current velocities partly result from varying instrument depth. The RCM is installed at about 24 m above the ground, i.e., within the plume during the whole moored record. In contrast, the ADCP is knocked down regularly during enhanced current speeds resulting in varying depth levels of the instrument between 75 and 125 m above the seafloor (Figure 8). Consequently, due to temporal changes in the ADCP depth but also in the plume thickness, the ADCP records velocities within the plume, within the interfacial layer, and within the ambient water at different times of the mooring record (Figure 8b).

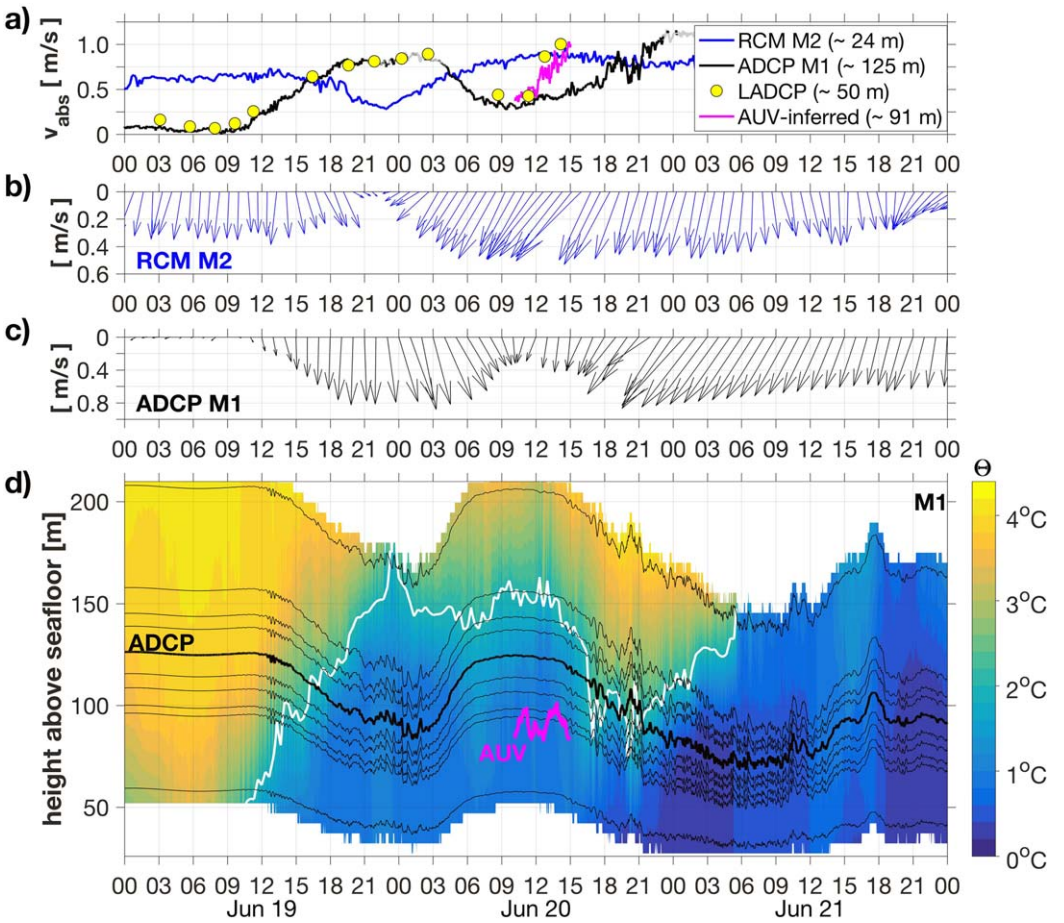

Figure 9. Moored time series data from 19 to 21 June 2012. (a) Absolute current speeds from the RCM (mooring site M2), the ADCP (mooring site M1), from LADCP profiles at 50 m above the seafloor (along the track of AUV dive B), and AUV-inferred from AUV dive B (see also map in Figure 2). (b and c) Both the current amplitude and current direction from the RCM at M2 and the ADCP at M1, respectively. Current vectors are rotated; vertically downward pointing arrows show downstream flow. Upslope and downslope flows are evident by clockwise and anticlockwise rotation of the arrows, respectively. For the RCM velocities we subtracted a mean background velocity of 0.3 m s^{-1}. (d) The time evolution of potential temperature at the M1 mooring (see Figure 8 for further explanations). Black lines mark the altitude levels of the MC sensors and the ADCP; the magenta line represents the altitude level of the AUV during dive B.

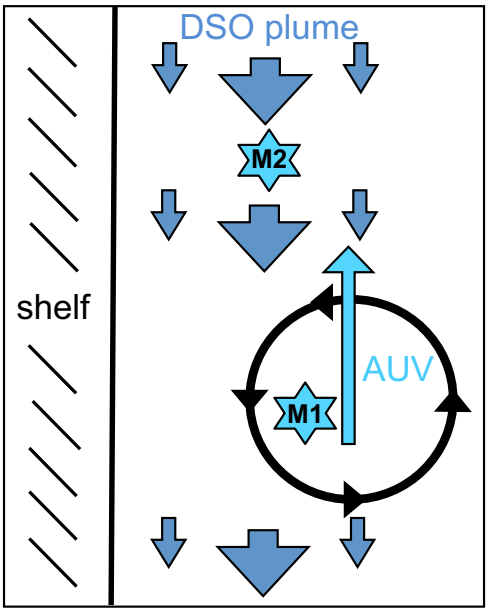

Figure 10. Sketch of a cyclonic eddy advected downstream by the DSO plume (blue arrows) along the Greenland continental slope (left side). The light blue arrow indicates the AUV passing through the eddy. In addition, the location of mooring sites M1 and M2 are indicated by the stars.

3.2.5. Résumé

In the following, we will analyze moored and lowered CTD/ADCP data observed in June 2012 with particular focus on the time period of the turbulent event captured during AUV dive B. Not only current measurements from the LADCP profiles but also from moored instruments show an increase in plume velocities on 20 June by 0.5 to 0.9 m s^{-1} (Figure 9a). The best correlation between the velocity time series at M1 and M2 is found by shifting M2 by 10.5 h forward in time. This suggests a signal propagation velocity of v = (17.7 km/10.5 h) ≈ 0.47 m s^{-1} between the two mooring locations. We suggest this can be explained by an energetic mesoscale eddy being advected by the DSO plume. The eddy may cause both, the strong increase in current speeds and the enhanced levels of turbulence. The AUV traveled from the central mooring M1 toward the upstream site M2 at the same time (Figure 9a). Thus, the AUV should have captured the same signal as observed by the moored devices. However, the AUV should observe a stronger velocity change rate ($\delta v/\delta t$), because it traveled against the direction of the propagating eddy. The observations agree with these expectations (Figure 9a).

The passage of an eddy should be reflected by a change in the direction of the flow. Indeed, the measurements at M1 indicate that the plume velocities turned toward the shelf during the increase in current speeds on 20 June (Figure 9c). In contrast, earlier on 20 June, from 0:00 to 10:00 UTC, the velocities show a decrease in current speeds from 0.9 to 0.4 m s^{-1} and an offshore component. The decrease in current speeds between the offshore and onshore velocities is indicative for the passage of a cyclonic eddy and cannot be explained by meandering motion of the plume. Vectors from the RCM located further upslope at M2 (see Figure 2) and close to the seafloor (24 m) show a similar behavior but 10.5 h earlier (Figure 9b). During the time of intensified flow (19 June, 15:00 UTC until the end of the record) the moored temperature data show a thickening of the DSO plume, as suggested by the presence of water with temperatures lower than 2°C (Figure 9d). Coinciding with the onset of stronger flow (most likely caused by the trailing edge of the eddy) high-frequency variability is seen in the pressure records of the moored sensor at M1 between 17:00 and 23:00 on 20 June (Figure 9d). This suggests the presence of high-frequency velocity fluctuations. At the same time moored temperature data show the intrusion of warmer water into the DSO plume (Figure 9d). This is consistent with the AUV observations (Figures 5 and 7). Our interpretation thus is that the AUV was launched inside the eddy in relatively low velocities and subsequently traveled upstream toward the trailing edge of the eddy (illustrated in Figure 10). During the transition from low to high plume velocities associated with the downstream translation of the eddy, enhanced dissipation rates and temperature variance were captured by the AUV (Figures 5 and 7). At the same time critical *Ri* numbers and an enhanced vertical shear of horizontal velocities were observed based on lowered CTD/LACDP profiles (Figures 4d and 4e).

We interpret this as follows: the eddy acts in exchanging water laterally between the plume and the ambient water, advecting warm water from offshore toward the plume area on its trailing edge (Figure 9). The eddy-induced increase in flow speeds coincide with increased velocity shear and provides mechanical energy required for the enhanced dissipation, thus facilitating the mixing of the warm ambient water into the plume. We will come back to this interpretation in the discussion.

3.3. Evidence for Intense Mixing Across the Interfacial Layer Driven by Flow-Topography Interaction

A high resolution topographic chart acquired by a multibeam echo sounder survey in June 2012 highlights an isolated, circular feature of 100 m height at 30°0.0′W and 65°12.5′N (Figure 2). This topographic feature is not represented in standard bathymetry products like the 1-Minute Gridded Global Relief Data (ETOPO1)

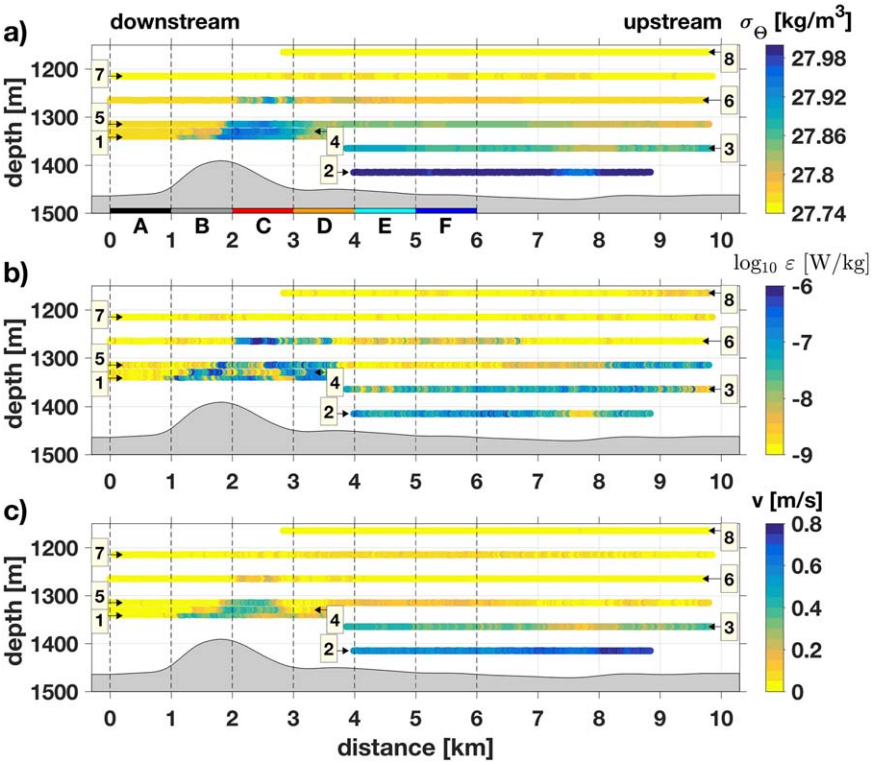

Figure 11. (a) Potential density, (b) dissipation rate, and (c) AUV-inferred current velocity observed during AUV dive A (12 June, 23:10 to 13 June, 9:50) at constant depth levels. The succession of starting points of the different legs is marked by the framed numbers, the arrows denote in which direction the AUV was heading throughout each leg. Gray shading denotes the bottom topography. In all plots, the horizontal axes show the horizontal distance of the AUV to the southwestern-most point of leg 6. Colored lines at the bottom of Figure 11a indicate distance intervals used in Figure 12.

[*Amante and Eakins*, 2009] (Figure 2). The topographic elevation has a diameter of 2 km giving rather smooth 8% slopes on its upstream and upslope side, while the slopes on the opposite side, i.e., downstream and downslope, are twice as steep. Owing to the small horizontal length scale of the topographic obstacle of O(10^3) m and the fast flow of the plume of O(1) m s^{-1} (Figure 11) rotational effects most likely can be excluded (Rossby number $R_0 = 10$, nonrotating problem). The plume is therefore expected to flow over the hill rather than around it.

While the AUV followed the 1475 m isobath during dive A it passed the northwestern part of this topographic elevation. In the following, we analyze AUV-based measurements obtained during dive A with respect to this elevation. If found to be a mixing hotspot, isolated plume-topography interaction might represent an important mechanism of entraining warm ambient water into the plume.

3.3.1. Plume Hydrography, Dissipation Rates, and Current Speeds

As revealed by Figure 11, the horizontal AUV legs of dive A covered the vertical plume structure, i.e., (i) the dense, well-mixed core of the DSO plume (leg 2; cold and fresh ($\Theta \approx 0.5$°C, $S = 34.90$), not shown), (ii) the interfacial layer featuring a strong density gradient (legs 1, 3, 4, 5), and (iii) the ambient water (legs 6, 7, 8; warm and saline ($\Theta \approx 4.2$°C, $S = 34.96$–34.98), not shown). Dissipation rates with mean values of O(10^{-7}) W kg^{-1} and downstream current speeds between 0.6 and 0.8 m s^{-1} are observed within the plume (Figure 11), which are in striking contrast to the values obtained in the ambient water higher up in the water column (leg 8; ε = O(10^{-9}) W kg^{-1}; downstream current speeds of 0.1 m s^{-1}).

An intrusion of dense plume water into the more saline and warmer ambient water was found in the distance interval between 1.5 and 3.5 km, i.e., above the topographic elevation (Figure 11). Here also highly elevated dissipation rates peaking at 10^{-6} W kg^{-1} over a horizontal scale of 500 m and enhanced plume speeds can be observed. In order to distinguish whether the elevated dissipation rates and densities result from intrusions (entrainment) or simply arise from the plume flowing over the topographic elevation, we analyzed mean densities and dissipation rates obtained during AUV dive A with respect to height above

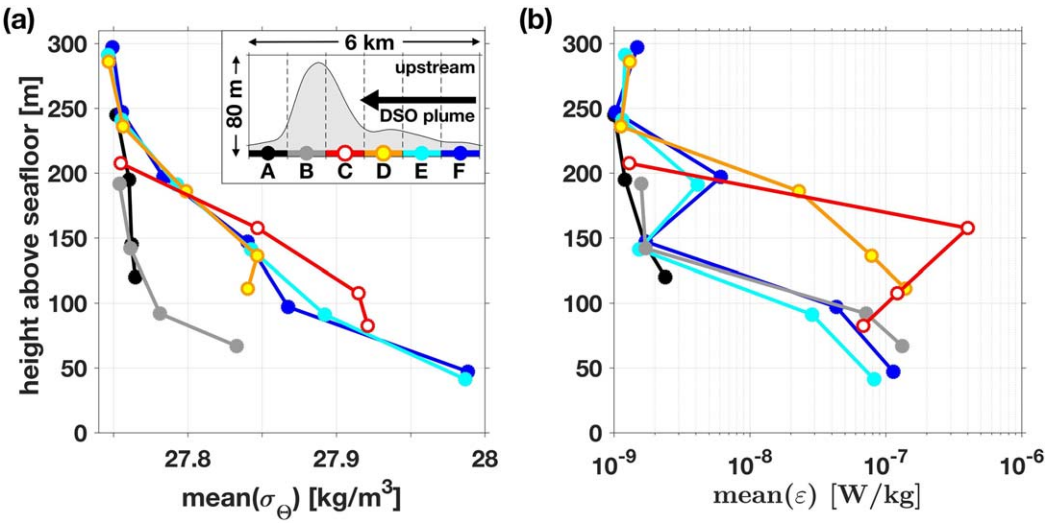

Figure 12. (a) Mean vertical profiles of potential density and (b) dissipation rates as a function of height above the seafloor based on observations from AUV dive A (see also Figures 11a and 11b). Mean properties were calculated along the legs within given distance intervals as marked in the legend (see Figure 11a for comparison).

the seafloor. We chose six 1 km long segments along the section (marked in Figures 11a) covering different regimes with respect to the topographic obstacle. Segment A is located downstream the obstacle (0–1 km), segments B and C right at the obstacle on its downstream (1–2 km) and upstream side, respectively (2–3 km), and segments D, E, and F reside further upstream of the obstacle (3–6 km). Within each segment we derived mean properties along the corresponding AUV legs. The height above seafloor was derived from the difference between the mean depth of the AUV leg and the mean bottom depth within the corresponding segment. The results indicate that the higher densities penetrate well above the DSO plume into the water column in segment C, i.e., right above the upstream slope of the elevation (Figure 12a). Within the same segment we observe enhanced dissipation rates of O(10^{-7}) W kg^{-1} between 100 and 160 m above the seafloor (Figure 12b). Since the fast flowing plume is less than 100 m thick prior to encountering the obstacle, we conclude that the elevated dissipation rates and densities in segment C are a result of intrusions driven by flow-topography interaction rather than simply a manifestation of the plume.

The cold and fresh intrusion is present along legs 1, 4, 5, and 6 (Figure 11) although they were obtained up to 6 h apart from each other (Table 2). Consequently, the localized turbulent patch was not advected downstream by the plume but kept its position on the upstream side of the hill for the duration of at least 6 h (advection by a moderate plume velocity of 0.4 m s^{-1} would have moved it downstream by 10 km in this time span).

Downstream of the elevation, i.e., in the distance interval between 0 and 1 km, we did not resolve the vertical plume structure. Here, between 120 and 250 m above the seafloor the water is rather homogeneous throughout all legs (Figure 11).

LADCP measurements taken at the same time but slightly off from the AUV track and 2.8 km away from the topographic elevation (Figures 2 and 4) indicate an increase in plume velocities but we did not find indications of a change in current direction here (not shown). Thus our observations obtained during dive A are most likely not associated with the passage of an eddy. The AUV observations can be partly explained by the spilling of dense water over the top of the elevation. Nevertheless, this does not explain the enhanced dissipation rates reaching up to 160 m above the highest point of the elevation. Our results imply stationary, localized flow-topography interaction driving enhanced mixing at the upstream side of the obstacle. This aspect will be taken up again in the discussion.

3.3.2. Entrainment Rates

Based on the assumption that the observed turbulence upstream the topographic elevation was a stationary feature (over the duration of the dive), we calculate entrainment rates from our AUV measurements. The entrainment rate, w_e, is defined as the temporal change in the bulk thickness, H, of the gravity current ($w_e \equiv \partial H/\partial t$). Following *Arneborg et al.* [2007] it can be expressed by

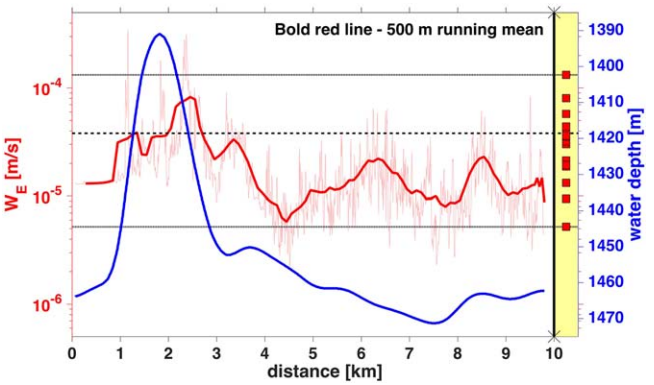

Figure 13. Entrainment rates (w_e, thin red line) along AUV dive A in comparison to w_e published in *Paka et al.* [2013] from the same study area but taken slightly upslope and upstream of AUV dive A (yellow shaded box). The thick red line gives the 500 m running mean (100 m overlap). Shown in blue is the water depth along the track interpolated based on the multibeam survey obtained during cruise MSM21/1b (see Figure 2). The red squares show entrainment rates based on the vertical microstructure profiles described in *Paka et al.* [2013]; the black dashed line indicates the mean, the dotted black line the upper and lower limits of all w_e obtained from the vertical microstructure profiles.

$$w_e = 2\int_0^\infty F_b dz \Big/ \int_0^\infty g' dz \qquad (2)$$

where $F_b = g\langle w'\rho'\rangle/\rho_0$ is the buoyancy flux, $g' = g(\sigma_\Theta(z) - \sigma_\Theta(\infty))/\rho_0$ is the reduced gravity, w' and ρ' are turbulent fluctuations of vertical velocity and density, respectively, ρ_0 is the reference density, and g is gravity acceleration; the z axis is directed upward with $z = 0$ at the seafloor. In the stably stratified interface layer of the gravity current the buoyancy flux can be expressed through dissipation rate by $F_b = 0.2\varepsilon$ [*Osborn*, 1980], while in the neutrally stratified near-bottom mixed layer, where the potential density is vertically uniform, F_b changes linearly with z (with $F_b = 0$ at $z = 0$). In practice, instead of $z = \infty$ in equation (2) one has to take some z level above the gravity current, and the calculated value of w_e is not expected to be highly sensitive to the choice of the upper integration limit due to relative smallness of ε and $\partial\sigma_\Theta/\partial z$ above the gravity current. We computed the entrainment rate, taking $F_b = 0.2\varepsilon$, by linear vertical interpolation between the measured dissipation rates and potential densities during AUV dive A. At the seafloor we set $\sigma_\Theta = 28.029$ kg m^{-3}, corresponding to near-bottom values along AUV leg 2, and $F_b = 0$. The data measured along AUV leg 7 were taken for the upper integration limit. To our minds, the main source of errors of the calculated entrainment rates lies in linear vertical interpolation between the measured dissipation rates, because the vertical profiles of ε are known to be highly variable (patchy) due to turbulence intermittency [e.g., *Paka et al.*, 2013]. For this reason, it is hardly expected that the accuracy of the w_e estimates is better than one order of magnitude. Since we have no measurements at 50 m above the seafloor at distance intervals of 0–4 km and 9–10 km, the missing data were filled by the mean values of ε and σ_Θ measured along AUV leg 2 between 4 and 9 km. The resulting entrainment rates yield values between 10^{-6} and 10^{-4} m s^{-1} and thus compare favorably with the ones calculated by *Paka et al.* [2013] based on vertical microstructure measurements obtained during the cruise in the same area between 13 and 20 June 2012 (Figure 13). Entrainment rates immediately upstream of the elevation are larger compared to the mean entrainment rate of $w_e = 3.8\times10^{-5}$ m s^{-1} computed by *Paka et al.* [2013]. However, they did not obtain dissipation measurements right at the obstacle, such that a direct comparison is not feasible. In contrast, the entrainment rates show up to 3 times smaller values away from the topographic elevation (Figure 13). Downstream of the obstacle, the entrainment rate is very small (Figure 13). Here the AUV was not sailing in the boundary layer of the overflow, but just in rather homogeneous ambient water above the plume. Thus, entrainment rates are likely underestimated here.

The entrainment rates based on our observations are not significantly greater than the estimated uncertainty. Nonetheless, if the pattern implied by our data is robust and entrainment rates increase near the obstacle, this implies that ambient water is entrained into the DSO plume due to flow-topography interaction at the 100 m high topographic elevation. This might be in agreement with the lower density values observed downstream of the elevation in the interfacial layer. No downstream AUV-based density observations were made within the plume, however, such that changes in plume properties can unfortunately not be documented.

4. Discussion

4.1. Enhanced Turbulence Driven by Mesoscale Motions

The observations presented in this study originate from a small area within the DSO plume near its offshore edge. We found two mechanisms promoting strong mixing in the interfacial layer above the plume, with

one interpreted as a transient mesoscale bottom-intensified eddy and the other relating to the interaction between the plume and a topographic obstacle with horizontal and vertical scales of less than 2 km and 100 m, respectively.

Several studies discussed that pulses of dense overflow water (called "boluses") can be associated with cyclonic eddies traveling with the DSO plume downstream along the East Greenland continental slope [e.g., *Bruce*, 1995; *Spall and Price*, 1997; *Käse et al*., 2003]. Recently, both the velocity and density structures and the frequency of cyclonic eddies on the East Greenland continental slope passing a mooring array near 33°W—just 140 km downstream of our working area—were investigated by *von Appen et al*. [2014]. Their observations suggest the maximum frequency of the cyclonic eddies (0.5 per day) to occur just onshore of the onshore edge of the plume at the 900 m depth contour (mooring 4 of their array). Bottom densities at the next offshore mooring (at 1160 m) only episodically reached values in excess of 27.85 kg m^{-3} (i.e., densities of the DSO plume). The cyclones reported on by *von Appen et al*. [2014] propagated faster than disturbances in the sea surface temperature field obtained from satellite infrared measurements with 1 km spatial resolution. Based on that, *von Appen et al*. [2014] proposed that DSO cyclones cannot be directly related to surface signatures. Likewise we do not find evidence of a surface expression of the mesoscale features we observed. We believe that the eddy we observed shares common features with the eddies described by *von Appen et al*. [2014], i.e., the eddies are cyclonic and have no surface expression. Nevertheless, most of the eddies described in *von Appen et al*. [2014] occur onshore of the plume while our observed feature 140 km upstream is rather found offshore of the plume and shows higher core densities (see Figure 5a). Our results connect the presence of a bottom-intensified mesoscale eddy with a dense bolus at depth. While both the onshore and offshore features reported by *von Appen et al*. [2014] and from this study, respectively, may possibly share the same mechanism of generation (vortex stretching of the plume), the different depth structure and location of occurrence (onshore versus offshore edges of the plume) suggests that the two features may actually not be linked.

Our observations suggest that the eddy we observed may foster entrainment in two ways. First, it promoted the advection of offshore warm water toward the plume. Second, as a result of the enhanced vertical shear of horizontal velocity associated with the eddy, Kelvin-Helmholtz type instabilities may have occurred to produce the observed intense vertical mixing. The role of mesoscale variability in the plume may therefore not just be restricted to lateral exchanges (i.e., the advection of warm water toward the plume), but may also extend to largely enhancing vertical mixing during times, when warm water is advected toward the plume. The significance of eddies for the entrainment will certainly not be restricted to the DSO plume. Observations obtained by *Fer et al*. [2010] in the Faroe Bank Channel overflow show dissipation rates of up to $O(10^{-5})$ W kg^{-1} during the passage of an eddy.

We are aware, that our observations are restricted to the passage of one mesoscale feature, and more observations and analyses are required to understand the significance of our results for the overall water mass transformation of the plume. Our moored time series of temperature and velocity—extending over 1.5 months—suggest a fairly regular passage of eddies to occur every 1.6 days (Figure 8). The eddy event discussed here, which is characterized by a change from offshore to onshore current components, a strong increase in plume velocities up to 1.1 m s^{-1}, a thickening of the plume, and enhanced turbulence, was found to occur about 7 times during the whole moored record, i.e., on weekly time scales (Figure 8). Figure 14 exemplary shows a second example of a similar eddy event observed between 18 and 20 July, which compares well with the former discussed eddy event passing the study area about one month earlier (Figure 9).

With respect to our moored velocities we need to keep in mind that the moored instruments are knocked down during strong current speeds. During these times our ADCP time series does reflect on the plume velocity, while occasionally, i.e., during rather moderate plume speeds, the instrument is placed in the interface between the plume and ambient water (Figure 8b). Nevertheless, the RCM at M2 is placed within the DSO plume during the whole time due to its location further upslope (Figure 2) and close to the seafloor. Here we found similar eddy signatures, i.e., intensified plume speeds with current components changing from downslope to upslope within a day about 10.5 h before the signal is found in the ADCP time series (Figures 9 and 14). The moored temperature time series suggests that periods of strong eddy events (20 June to 8 July, and 18–27 July) alternate with periods of weak eddy events (9–17 July 2012) (Figure 8).

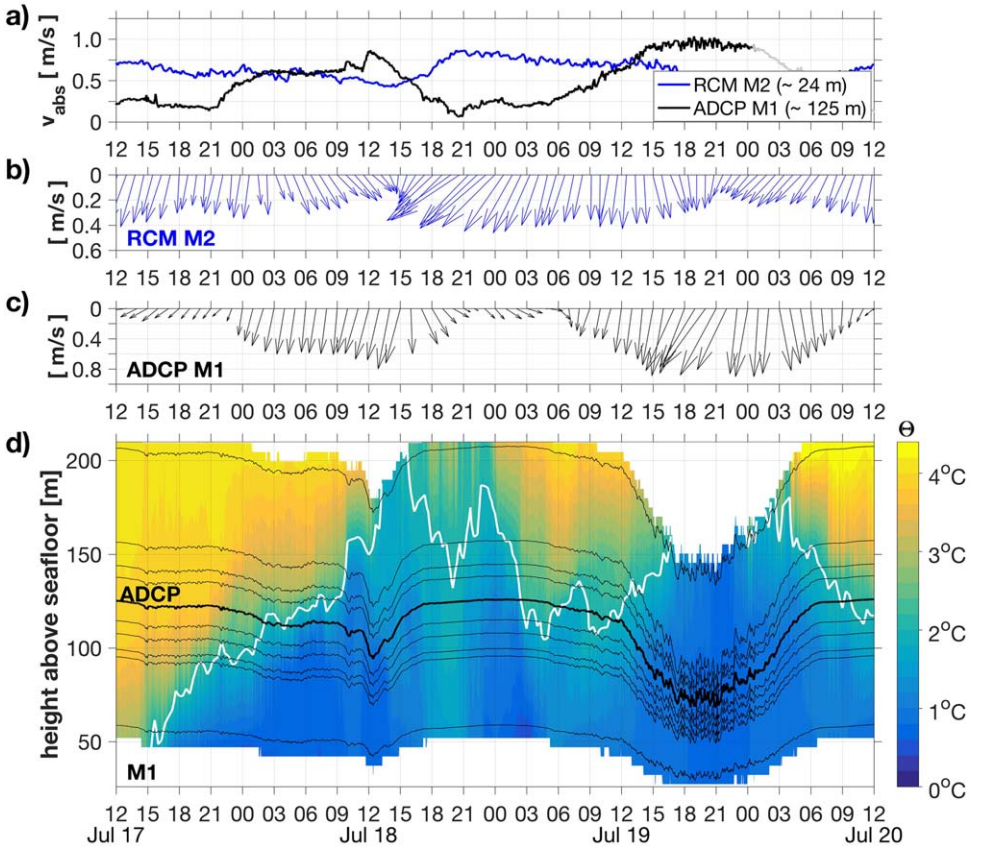

Figure 14. Moored time series data for an eddy event detected between 17 and 20 July 2012. (a) Absolute current speeds from the RCM (mooring site M2) and the ADCP (mooring site M1). (b and c) Both the current amplitude and current direction from the RCM at M2 and the ADCP at M1, respectively. Current vectors are rotated; vertically downward pointing arrows show downstream flow. Upslope and downslope flows are evident by clockwise and anticlockwise rotation of the arrows, respectively. For the RCM velocities we subtracted a mean background velocity of 0.3 m s^{-1}. (d) The time evolution of potential temperature at the M1 mooring (see Figure 8 for further explanations). Black lines mark the altitude levels of the MC sensors and the ADCP. The white line denotes the 2° isotherm.

This may be linked to the meandering motion of the plume; however due to the complexity of the system other processes beyond the scope of this paper may also play a role.

AUV-based measurements during dive B in the interfacial layer above the DSO plume showed that periods of enhanced dissipation rates occurred at the same time as we observed strong temperature variance in the inertial-convective subrange of turbulence at wave numbers between 0.01 and 7 cpm. Our measurements in a less energetic regime implied a wave number dependence characteristic in the inertial-convective subrange of turbulence at wave numbers between 0.04 and 3 cpm. This is consistent with results obtained by the same observing system in a less turbulent environment in the central valley of the Mid-Atlantic Ridge [*Tippenhauer et al*., 2015], where the transition from the inertial-convective to the inertial-diffusive band was revealed to occur at 1 cpm [*Tippenhauer et al*., 2015]. This might imply that in our study, the transition between the two subranges is shifted to higher wave numbers, as a result of the larger turbulence levels found here. If the transition occurs at a sufficiently large wave number in excess of 7 cpm, then it may simply not have been resolved by the thermistor.

Notably, the low-wave number limit of the inertial-convective subrange in the study by *Tippenhauer et al*. [2015] occurred near 0.004 cpm. Here we found a transition to the internal-wave subrange in the least energetic regimes at wave numbers smaller than 0.04 cpm. This favorably compares to the towed observations obtained by *Klymak and Moum* [2007a] for the upper ocean. The authors point out that turbulence existing at horizontal scales of this size is expected to be anisotropic (with the corresponding vertical scales being significantly smaller than the horizontal ones obtained here), and we highly recommend consulting their excellent review on this matter. Interestingly, they refer to studies by *Smyth et al*. [2001], *Seim and Gregg*

[1997] and *Moum et al*. [2003] which all suggest that Kelvin-Helmholtz instabilities should produce turbulence with larger horizontal than vertical scales. Given the large vertical shear in horizontal velocity we observed during the occurrence of strongest dissipation, we expect Kelvin-Helmholtz instabilities to be an important driver of the mixing. This might then also explain the occurrence of the large horizontal scales of turbulence as revealed by the isotherm slope spectra in our study.

Both the vertical high-frequency oscillations of the mooring (Figure 9d) and the slope spectra (Figure 7) suggest the presence of internal waves. For a two-layer case with reasonable scales of layer thickness, we estimated phase velocities between 0.4 and 0.5 m s^{-1} for our settings. The role of internal waves in the supply of energy to turbulence in the DSO plume is unknown yet but might be significant. A fair amount of energy from the mesoscale eddies present in the DSO plume could be fluxed into the internal wavefield [e.g., *Polzin*, 2010], with the latter supplying energy to turbulence. This is supported by *Seim and Fer* [2011] who observed high levels of energy in the internal wavefield within the thick stratified interfacial layer on top of the Faroe Bank Channel overflow, which shares common characteristics with the DSO plume.

During the descent of the plume the potential energy of the dense plume water is in part converted to eddying, vertically sheared motions (kinetic energy), that laterally advect heat toward the plume. At the same time. it provides a source of mechanical energy to introduce intense vertical mixing. The latter should ultimately result in a decay of the eddies, and the turbulent kinetic energy produced will in part be converted to potential energy. Our observations may be interpreted such that they provide evidence for at least parts of the energy conversions taking place. The eddy-related large velocities (and velocity shear) occurring on a spatial scale of several kilometers coincided with elevated energy found across the internal-wave and inertial-convective subranges and beyond.

If entrainment elevated by enhanced turbulence is linked to the passage of mesoscale eddies, the huge spatial-temporal variability of mixing should make the interpretation of a limited number of point measurements of dissipation (as carried out by *Paka et al*. [2013]) in terms of entrainment by vertical mixing into the DSO plume rather challenging. Our data unfortunately does not allow us to compute entrainment velocities during AUV dive B, i.e., during the passage of the eddy, when dissipation rates were largest, as measurements were only obtained at one depth level. Neither did *Paka et al*. [2013] take vertical profiles of dissipation during dive B. The discrepancies between the large-scale approaches of estimating lateral entrainment such as by *Voet and Quadfasel* [2010], the small-scale observations of vertical mixing by *Paka et al*. [2013] and the high resolution ocean model study by *Koszalka and Haine* [2013] will be partly due to not adequately resolving the processes related to the temperature fluxes (or entrainment velocities) in time and space.

4.2. Enhanced Turbulence Driven by Flow-Topography Interaction

Many studies show the occurrence of elevated mixing in (stationary or transient) hydraulically controlled situations on the downstream side of obstacles, close to where the transition from supercritical to subcritical flows takes place (see recent observations in the deep ocean at mid-oceanic ridge systems by *Alford et al*. [2013] and *Tippenhauer et al*. [2015]). Our observations did not resolve the downstream part of the studied topographic elevation where supercritical plume conditions are likely to occur. We instead observed strongly enhanced turbulence upstream of a topographic elevation reaching far above its crest and extending over a vertical scale in excess of the height of the elevation. Studies on tidal flows in fjords encompassing sills relying on both observations and numerical simulations have shown the generation of bores over topography from which trains of internal waves develop that subsequently propagate upstream during the slackening tide [e.g., see *Cummins et al*., 2003, and references therein]. A possible explanation for the strongly enhanced turbulence observed upstream of a topographic elevation encountered by the DSO plume on the continental slope could be an interaction of the plume with internal gravity waves excited at the upstream side of the elevation.

Legg [2014] investigated the spatial patterns of turbulent dissipation arising from the breaking of low-mode internal waves at isolated topography. The author varied both the crest height and the steepness of the topographic slope relative to the slope of the group velocity of the internal waves impinging onto the topography. For some of the parameter settings, the spatial patterns of dissipation share remarkable similarities with the observations from the elevation shown in this study, with dissipation being most pronounced on that side of the isolated topography, onto which the internal wave impinges, and with the area of elevated dissipation extending well above the crest. This is the case also for relatively small crest heights

(compared to water depth). For the quasi-stationary DSO plume (over the 6 h period of our observations) this may suggest that internal waves were generated or reflected at the elevation and subsequently propagated upward and upstream (i.e., against the mean flow) where they might become arrested by the counter-flow and eventually break to cause the observed elevated turbulence on the upstream side of the topographic elevation. The reduced level of turbulence downstream of the elevation could imply that the waves are eroded by the mean flow. Alternatively, the flow may indeed have been turbulent downstream (likely due to supercritical conditions) with the AUV not resolving this situation as no leg was carried out close to the seafloor downstream of the topographic elevation. Our observations are certainly not ideal to resolve the vertical distribution of turbulence downstream of the elevation. The analysis is further limited because there are no observations in the cross plume direction across the topographic elevation. In order to gain a better insight and test the stationarity of the observed feature, there would be the need for higher temporal-spatial resolution observations in the vicinity of such topographic elevations.

5. Conclusion

The operation of a horizontally profiling AUV made it possible to carry out measurements of small-scale time and space variability of hydrographic properties, velocity, and turbulent kinetic energy in the interfacial layer above the DSO plume about 180 km downstream from the sill in Denmark Strait. The AUV-based data set showed two major events of strong temperature fluctuations and enhanced dissipation rates of O(10^{-6}) W kg^{-1}.

The first turbulent event was linked to the passage of an energetic eddy with the AUV most likely encountering the trailing edge of it. Enhanced dissipation rates of O(10^{-6}) W kg^{-1} were observed compared to O(10^{-9}) W kg^{-1} at the beginning of the dive. The high dissipation coincided with high small-scale horizontal temperature variances. High turbulent mixing was also suggested based on both lowered CTD/ADCP measurements of critical *Ri* numbers and large vertical shear of horizontal velocity, and pronounced high-frequency temperature and pressure fluctuations observed by moored instruments. In addition, moored velocity data indicated the advection of ambient water toward the shelf. Consequently, both the onshore advection of ambient water by the eddy and the vertical mixing seemed to act in concert causing an efficient entrainment of ambient water through the interfacial layer into the DSO plume. We propose that the vertical mixing was induced by the large vertical shear of horizontal velocity of this bottom-intensified eddy. It remains to be seen in future analyses, how representative our observations for the occurrence of this type of eddies are. If bottom-intensified eddies are found to occur frequently on the offshore edge of the plume, they might represent an efficient mechanism for the warming of the plume as they accomplish both the lateral advection and vertical mixing.

The horizontal scales of temperature variability during the passage of the eddy ranged from the lowest observed scales of 0.05–500 m. Isotherm displacement slope spectra were computed. They clearly revealed the characteristic slope of the inertial-convective subrange of turbulence in the wavelength range between 0.14 and 100 m. The transition to the inertial-diffusive subrange was, if at all, only detected during low turbulence. The slopes of the spectra were very consistent with each other for low, moderate and strong dissipation with the amplitude of the spectra varying according to the levels of dissipation.

The second turbulent event was observed upstream of a topographic elevation of about 100 m height and somewhat less than 2 km horizontal extent. Here the cold, and fresh plume water was observed to intrude into the overlying warm and saline ambient water. It seems that the localized turbulent patch was not advected downstream by the fast flowing plume (featuring flow speeds near 0.6 m s^{-1}) but kept its position on the upstream side of the elevation for the duration of at least 6 h. Elevated dissipation rates suggest that the flow-topography interaction may cause vertical mixing here. Accordingly, vertical entrainment velocities estimated from the vertical distribution of dissipation along the plume axis yielded maximum values on the upstream side of the elevation. The topographic elevation was not adequately represented in global high-resolution satellite-based topographic datasets such as ETOPO1. If a larger number of such undetected elevations, with similar possibly locally enhanced, quasi-stationary turbulent mixing exist along the pathway of the DSO plume, one may speculate that taken together they might significantly contribute to the entrainment of warm ambient water into the DSO plume by vertical mixing. The processes that establish the mixing upstream of the elevation rather than in the wake of it, are yet to be explored.

The enhanced dissipation observed by the AUV in the vicinity of a topographic elevation and near the edge of an eddy imply that entrainment by diapycnal fluxes will be intermittent in space and time. Nevertheless, if the observed features can be shown to be robust, they highlight mechanisms of significant localized entrainment of ambient water into the DSO plume. In future work, it should be studied whether these mechanisms are sufficient to explain the increase in the DSO plume in terms of both temperature and volume transport on its way downstream from the sill in Denmark Strait along the continental slope of Greenland. We are hopeful, that our observations may inform and stimulate both process-based and regional ocean numerical modeling experiments that might help to evaluate the importance of the highlighted mechanisms for sustaining the deep limb of the AMOC.

Acknowledgments

The research leading to these results has received funding from the European Union 7th Framework Programme (FP7 2007-2013) under grant agreement 308299 (NACLIM project) and the grant KA 3204/2-1 provided by the German Science Foundation. Ship time was granted by the German Science Foundation. We acknowledge the contribution of the captain and crew of the research vessels R/V *Maria S. Merian* and R/V *Poseidon*, and the AUV team (Marcel Rothenbeck, Jan Sticklus, and Momme Deutschmann) from GEOMAR. We thank Uwe Koy for the technical support and Gerd Krahmann for processing the CTD and LADCP data, and for providing Matlab routines for CTD quality control. We thank Johannes Hahn for providing Matlab routines and support for spectral and wavelet analysis. Nuno Nunes, Bert Rudels, Tim Fischer, and Vadim Paka are acknowledged for helpful discussions. Finally, we acknowledge two anonymous reviewers for their help in improving the manuscript. AUV-based, shipboard, and mooring data are available upon request from the authors (janin.schaffer@awi.de) or via the PANGAEA database (https://www.pangaea.de, doi:10.1594/PANGAEA.861352).

References

Alford, M. H., J. B. Girton, G. Voet, G. S. Carter, J. B. Mickett, and J. M. Klymak (2013), Turbulent mixing and hydraulic control of abyssal water in the Samoan passage, *Geophys. Res. Lett.*, *40*, 4668–4674, doi:10.1002/grl.50684.

Amante, C., and B. W. Eakins (2009), ETOPO1 1 arc-minute global relief model: Procedures, data sources and analysis, *NOAA Tech. Memorand. NESDIS NGDC-24*, Natl. Geophys. Data Cent., NOAA, Boulder, Colo., doi:10.7289/V5C8276M [01/10/2015].

Arneborg, L., V. Fiekas, L. Umlauf, and H. Burchard (2007), Gravity current dynamics and entrainment—A process study based on observations in the Arkona Basin, *J. Phys. Oceanogr.*, *37*, 2095–2113, doi:10.1175/JPO3110.1.

Bacon, S. (1997), Circulation and fluxes in the North Atlantic between Greenland and Ireland, *J. Phys. Oceanogr.*, *27*(7), 1420–1435, doi:10.1175/1520-0485(1997)027 < 1420:CAFITN>2.0.CO;2.

Bacon, S., and P. M. Saunders (2010), Notes and correspondence. The Deep Western Boundary Current at Cape Farewell: Results from a Moored Current Meter Array, *J. Phys. Oceanogr.*, *40*, 815–829, doi:10.1175/2009JPO4091.1.

Brearley, J., R. Pickart, H. Valdimarsson, S. Jonsson, R. Schmitt, and T. Haine (2012), The East Greenland Boundary Current System South of Denmark Strait, *Deep Sea Res., Part I*, *63*, 1–19, doi:10.1016/j.dsr.2012.01.001.

Bruce, J. (1995), Eddies southwest of the Denmark Strait, *Deep Sea Res., Part I*, *42*(1), 13–29, doi:10.1016/0967-0637(94)00040-Y.

Bryden, H., and S. Imawaki (2001), Ocean heat transport, in *Ocean Circulation and Climate*, edited by G. Siedler, J. Chrurch, and J. Gould, chap. 6.2, pp. 455–474, Academic, London.

Cummins, P., S. Vagle, L. Armi, and D. M. Farmer (2003), Stratified flow over topography: Upstream influence and generation of nonlinear internal waves, *Proc. R. Soc. London, Ser. A*, *459*, 1467–1487, doi:10.1098/rspa.2002.1077.

Dansgaard, W., et al. (1993), Evidence for general instability of past climate from a 250-kyr ice-core record, *Nature*, *364*(6434), 218–220, doi:10.1038/364218a0.

Dickson, R. R., and J. Brown (1994), The production of North Atlantic Deep Water: Sources, rates, and pathways, *J. Geophys. Res.*, *99*(C6), 12,319–12,341, doi:10.1029/94JC00530.

Falina, A., A. Sarafanov, H. Mercier, P. Lherminier, A. Sokov, and N. Daniault (2012), On the cascading of dense shelf waters in the Irminger Sea, *J. Phys. Oceanogr.*, *42*, 2254–2267, doi:10.1175/JPO-D-12-012.1.

Fer, I., G. Voet, K. S. Seim, B. Rudels, and K. Latarius (2010), Intense mixing of the Faroe Bank Channel overflow, *Geophys. Res. Lett.*, *37*, L02604, doi:10.1029/2009GL041924.

Fischer, J., et al. (2015), Intra-seasonal variability of the DWBC in the western subpolar North Atlantic, *Prog. Oceanogr.*, *132*, 233–249, doi:10.1016/j.pocean.2014.04.002.

Gargett, A. E., T. R. Osborn, and P. W. Nasmyth (1984), Local isotropy and the decay of turbulence in a stratified fluid, *J. Fluid Mech.*, *144*, 231–280, doi:10.1017/S0022112084001592.

Girton, J. B., and T. B. Sanford (2003), Descent and modification of the overflow plume in the Denmark Strait, *J. Phys. Oceanogr.*, *33*(7), 1351–1364, doi:10.1175/1520-0485(2003)033 < 1351:DAMOTO>2.0.CO;2.

Goodman, L., E. R. Levine, and R. G. Lueck (2006), On measuring the terms of the turbulent kinetic energy budget from an AUV, *J. Atmos. Oceanic Technol.*, *23*(7), 977–990, doi:10.1175/JTECH1889.1.

Hall, S., S. Dye, K. Heywood, and M. Wadley (2011), Wind forcing of salinity anomalies in the Denmark Strait overflow, *Ocean Sci.*, *7*, 821–834, doi:10.5194/os-7-821-2011.

Hansen, B., S. Østerhus, D. Quadfasel, and W. Turrell (2004), Already the day after tomorrow?, *Science*, *305*, 953–954, doi:10.1126/science.1100085.

Jochumsen, K., D. Quadfasel, H. Valdimarsson, and S. Jónsson (2012), Variability of the Denmark Strait overflow: Moored time series from 1996–2011, *J. Geophys. Res.*, *117*, C12003, doi:10.1029/2012JC008244.

Jochumsen, K., M. Köllner, D. Quadfasel, S. Dye, B. Rudels, and H. Valdimarsson (2015), On the origin and propagation of Denmark Strait overflow water anomalies in the Irminger Basin, *J. Geophys. Res.*, *120*, 1841–1855, doi:10.1002/2014JC010397.

Johnson, G. C., J. M. Toole, and N. G. Larson (2007), Sensor corrections for Sea-Bird SBE-41CP and SBE-41 CTDs, *J. Atmos. Oceanic Technol.*, *24*, 1117–1130, doi:10.1175/JTECH2016.1.

Kanzow, T. (2015), North Atlantic Ventilation—Cruise No. MSM 21/1b—June 9-June 22, 2012—Reykjavik (Iceland)—Reykjavik (Iceland), *MARIA S. MERIAN-Berichte, MSM21/1b*, 55 pp., DFG-Senatskommission fuer Ozeanogr., Hamburg, Germany, doi:10.2312/cr_msm21_1b.

Käse, R. H., J. B. Girton, and T. B. Sanford (2003), Structure and variability of the Denmark Strait Overflow: Model and observations, *J. Geophys. Res.*, *108*(C6), 3181, doi:10.1029/2002JC001548.

Klymak, J. M., and J. N. Moum (2007a), Oceanic isopycnal slope spectra. Part II: Turbulence, *J. Phys. Oceanogr.*, *37*, 1232–1245, doi:10.1175/JPO3074.1.

Klymak, J. M., and J. N. Moum (2007b), Oceanic isopycnal slope spectra. Part I: Internal waves, *J. Phys. Oceanogr.*, *37*, 1215–1231, doi:10.1175/JPO3073.1.

Koszalka, I. M., and T. W. N. Haine (2013), Fates and travel times of Denmark strait overflow water in the Irminger basin, *J. Phys. Oceanogr.*, *43*, 12,611–2628, doi:10.1175/JPO-D-13-023.1.

Legg, S. (2014), Scattering of low-mode internal waves at finite isolated topography, *J. Phys. Oceanogr.*, *44*(1), 359–383, doi:10.1175/JPO-D-12-0241.1.

Lueck, R. G. (1990), Thermal inertia of conductivity cells: Theory, *J. Atmos. Oceanic Technol.*, *7*, 741–755, doi:10.1175/1520-0426(1990)007 < 0741:TIOCCT>2.0.CO;2.

Macrander, A., R. H. Käse, U. Send, H. Valdimarsson, and S. Jónsson (2007), Spatial and temporal structure of the Denmark Strait Overflow revealed by acoustic observations, *Ocean Dyn.*, *57*, 75–89, doi:10.1007/s10236-007-0101-x.

Magaldi, M. G., and T. W. N. Haine (2015), Hydrostatic and non-hydrostatic simulations of dense waters cascading off a shelf: The East Greenland case, *Deep Sea Res., Part I*, *96*, 89–104, doi:10.1016/j.dsr.2014.10.008.

Moum, J. N., D. M. Farmer, W. D. Smyth, L. Armi, and S. Vagle (2003), Structure and generation of turbulence at interfaces strained by internal solitary waves propagating shoreward over the continental shelf, *J. Phys. Oceanogr.*, *33*, 2093–2112, doi:10.1175/1520-0485(2003)033 < 2093:SAGOTA>2.0.CO;2.

Nasmyth, P. W. (1970), Oceanic turbulence, PhD thesis, Univ. of British Columbia, Vancouver, Canada.

Oakey, N. S. (1982), Determination of the rate of dissipation of turbulent energy from simultaneous temperature and velocity shear microstructure measurements, *J. Phys. Oceanogr.*, *12*(3), 256–271, doi:10.1175/1520-0485(1982)012 <0256:>2.0.CO;2.

Osborn, T. R. (1980), Estimates of the local rate of vertical diffusion from dissipation measurements, *J. Phys. Oceanogr.*, *10*(1), 83–89, doi:10.1175/1520-0485(1980)010 < 0083:EOTLRO>2.0.CO;2.

Paka, V., V. Zhurbas, B. Rudels, D. Quadfasel, A. Korzh, and D. Delisi (2013), Microstructure measurements and estimates of entrainment in the Denmark Strait overflow plume, *Ocean Sci.*, *9*, 1003–1014, doi:10.5194/osd-10-1067-2013.

Polzin, K. L. (2010), Mesoscale eddy-internal wave coupling. Part II: Energetics and results from PolyMode, *J. Phys. Oceanogr.*, *40*(4), 789–801, doi:10.1175/2009JPO4039.1.

Quadfasel, D., and R. Käse (2007), Present-day manifestation of the Nordic Sea overflow, in *Ocean Circulation: Mechanisms and Impacts—Past and Future Changes of Meridional Overturning*, edited by A. Schmittner, J. C. H. Chiang, and S. R. Hemming, pp. 75–89, Geophys. Monogr. Ser., Washington, D. C.

Rudels, B., P. Eriksson, H. Grönvall, R. Hietala, and J. Launiainen (1999), Hydrographic observations in Denmark Strait in Fall 1997, and their Implications for the entrainment into the overflow plume., *Geophys. Res. Lett.*, *26*(9), 1325–1328, doi:10.1029/1999GL900212.

Rudels, B., E. Fahrbach, J. Meincke, G. Budéus, and P. Eriksson (2002), The East Greenland Current and its contribution to the Denmark Strait overflow, *ICES J. Mar. Sci.*, *59*, 1133–1154, doi:10.1006/jmsc.2002.1284.

Schaffer, J. (2013), Small-scale variability associated with mixing in the Denmark Strait Overflow plume based on horizontally profiling observations, Master's thesis, Christian-Albrechts-Universität zu Kiel. [Available at http://oceanrep.geomar.de/22406/1/Master_Thesis_Janin_Schaffer.pdf.]

Seim, H. E., and M. C. Gregg (1997), The importance of aspiration and channel curvature in producing strong vertical mixing over a sill, *J. Geophys. Res.*, *102*, 3451–3472, doi:10.1029/96JC03415.

Seim, K. S., and I. Fer (2011), Mixing in the stratified interface of the Faroe Bank Channel overflow: The role of transverse circulation and internal waves, *J. Geophys. Res.*, *116*, C07022, doi:10.1029/2010JC006805.

Smyth, W. D., J. N. Moum, and D. R. Caldwell (2001), The efficiency of mixing in turbulent patches: Inferences from direct simulations and microstructure observations, *J. Phys. Oceanogr.*, *31*, 1969–1992, doi:10.1175/1520-0485(2001)031 <1969:TEOMIT>2.0.CO;2.

Spall, M. A., and J. F. Price (1997), Mesoscale variability in Denmark Strait: The PV outflow hypothesis, *J. Phys. Oceanogr.*, *28*, 1598–1623.

Taylor, G. I. (1935), Statistical theory of turbulence, *Proc. R. Soc. London, Ser. A*, *151*, 421–444.

Tippenhauer, S., M. Dengler, T. Fischer, and T. Kanzow (2015), Turbulence and fine structure in a deep ocean channel with sill overflow on the mid-Atlantic ridge, *Deep Sea Res., Part I*, *99*, 10–22, doi:10.1016/j.dsr.2015.01.001.

Torrence, C., and G. P. Compo (1998), A practical guide to wavelet analysis, *Bull. Am. Meteorol. Soc.*, *79*, 61–78, doi:10.1175/1520-0477(1998)079 < 0061:APGTWA>2.0.CO;2.

Våge, K., R. Pickart, M. Spall, H. Valdimarsson, S. Jónsson, D. Torres, S. Østerhus, and T. Eldevik (2011), Significant role of the North Icelandic Jet in the formation of Denmark Strait Overflow Water, *Nat. Geosci.*, *4*, 723–727, doi:10.1038/NGEO1234.

Visbeck, M. (2002), Deep velocity profiling using lowered acoustic doppler current profilers: Bottom track and inverse solutions, *J. Atmos. Oceanic Technol.*, *19*, 794–807, doi:10.1175/1520-0426(2002)019 < 0794:DVPULA>2.0.CO;2.

Voet, G., and D. Quadfasel (2010), Entrainment in the Denmark Strait overflow plume by meso-scale eddies, *Ocean Sci.*, *6*, 301–310, doi:10.5194/osd-6-2625-2009.

von Appen, W., R. Pickart, K. Brink, and T. Haine (2014), Water column structure and statistics of Denmark Strait Overflow Water cyclones, *Deep Sea Res., Part I*, *84*, 110–126, doi:10.1016/j.dsr.2013.10.007.

Yamazaki, H., and T. R. Osborn (1990), Dissipation estimates for stratified turbulence, *J. Geophys. Res.*, *95*(C6), 9739–9744, doi:10.1029/JC095iC06p09739.